Thin-Film Flows on Rotating Noncircular Cylinders with Large Curvature Variations

Chance Parrish,[1] Marcio S. Carvalho,[2] and Satish Kumar[1,*]

[1]Department of Chemical Engineering and Materials Science, University of Minnesota, Minneapolis, MN 55455, USA

[2]Department of Mechanical Engineering, Pontificia Universidade Católica do Rio de Janeiro, Rio de Janeiro, Rio de Janeiro 22451-900, Brazil

The coating of rotating objects with varying surface curvature is an important manufacturing step for a wide variety of products. To efficiently examine the flow of liquid coatings on such objects, we develop a lubrication-theory-based model for flow on 2D cross sections of rotating noncircular cylinders whose variations in the radius of curvature are comparable to the characteristic cylinder radius. Good quantitative agreement is found between model predictions and Galerkin finite-element method simulations when the coating thickness is small, whereas qualitative agreement is found for thicker coatings. Encouraged by this agreement, we conduct a parametric study to examine coating behavior on rotating elliptical cylinders. Four regimes of coating behavior are found spanning gravity-dominated and surface-tension-dominated regimes. The parameter space yielding smooth coatings on elliptical cylinders is small, suggesting the need for additional steps such as the addition of surfactant to widen this coating window.

*Email address for correspondence: kumar030@umn.edu

1. Introduction

The coating of discrete objects with varying surface curvature is an important manufacturing step for a wide variety of products such as medical devices and endoprostheses, rotationally molded or dip molded objects, and microelectronic devices [1–9]. In such applications, thickness variations in the coating may yield defective products with undesirable properties. However, when large curvature variations are present on an object's surface, controlling coating behavior may be difficult due to the complicated object shape and the large number of competing forces acting on the coating.

The flow of a thin coating on a circular cylinder rotating about its horizontal axis is a model problem commonly used to study flows on rotating discrete objects [10, 11]. In the earliest work on this subject, Moffatt [12] and Pukhnachev [13] examined coating behavior on two-dimensional cross sections of circular cylinders, neglecting flows along the horizontal axis. Using a definition of the load A per unit length of cylinder,

$$A = \int_0^{2\pi} \left[(R+H)^2 - R^2 \right] d\theta, \tag{1.1}$$

Moffatt developed an expression for the maximum load supported per unit length of cylinder in the absence of surface tension and inertia [12],

$$A_c^{circular} = \frac{1.057}{\gamma^{0.5}} \left(\frac{4\pi}{3} \right), \tag{1.2}$$

where the Stokes number $\gamma = \rho g R / \mu \Omega$ describes the ratio of gravitational forces to viscous forces. Here, μ is the liquid viscosity, Ω is the cylinder rotation rate, ρ is the liquid density, g is the gravitational acceleration, R is the cylinder radius, and H is the mean coating thickness. Below $A_m^{circular}$, a smooth, steady coating can be supported by cylinder rotation [12]. Above $A_c^{circular}$, fluid drains toward the underside of the cylinder, and axially spaced hanging droplets form and may be periodically shed [10, 12, 29]. By considering higher-order corrections to $A_m^{circular}$, Kelmanson [14] obtained an expression for the critical load which yields good agreement with experiments over a wider range of parameters than Eqn. (1.2).

In some cases, the objects being coated possess nonuniform surface curvature which may

drive the growth of thickness variations. Subsequent investigations have addressed this challenge by examining flows on noncircular cylinders [15, 16, 24, 25]. Hunt [15] explored coating behavior on 2D cross sections of elliptical cylinders using simulations of Stokes equations in the absence of surface tension. While steady solutions could not be obtained due to the cylinder shape, quasi-steady solutions could be obtained where cylinder rotation supports a fairly smooth coating on the cylinder surface [15]. Hunt [15] found that an increase in the major axis length a relative to the minor axis length b decreased the maximum liquid load A_m^{ellip} supported by cylinder rotation compared to the circular-cylinder value predicted by Kelmanson [14].

Li *et al.* [16] expanded on Hunt's work [15] by exploring surface-tension effects on the evolution of coatings on elliptical cylinders. Using 2D Galerkin finite-element method (GFEM) simulations of Stokes equations, Li *et al.* examined how capillary-pressure gradients due to the varying curvature of the elliptical cylinder drive evolution of the coating, providing snapshots of coating behavior as parameters such as the liquid load A and cylinder aspect ratio $\delta = b/a$ are changed [16]. While this study provides useful information, the computational cost associated with the GFEM simulations prevented a comprehensive parametric study [16]. A key goal of this work is to develop a reduced-order model for flows on elliptical cylinders, and more generally noncircular cylinders, so that parametric studies of coating behavior on such cylinders may be efficiently conducted.

One approach to examine such flows, outlined by Roy *et al.* [17] and Roberts & Li [18], is to use curvilinear coordinates that lie along the principal directions of the substrate, with the coating depth lying along the outward normal to the substrate [17, 18]. Here, a lubrication-theory-based model for flow on arbitrarily curved objects may be obtained, allowing a significant reduction in computational costs compared to GFEM simulations. Although this approach is powerful when studying coating flows on arbitrarily curved substrates [17–19], the geometric description of the coating breaks down when the coating thickness over concave regions of the substrate is larger than the substrate's principal radius of curvature [17, 18, 20, 21]. While a model for thin-film-flow on elliptical cylinders could be developed using the approach of Roy *et al.* [17], such an approach could not be generalized to study coating behavior on noncircular cylinders with highly curved concave regions, such as for sinusoidally patterned cylinders with large pattern amplitude.

An alternative approach is to study coating behavior in a curvilinear coordinate system lacking concave regions (e.g., cylindrical, spherical, or hyperbolic coordinates), allowing for convenient parameterization of the substrate and free-surface positions [20, 22–25]. Li *et al.* [24] and Parrish *et al.* [25] considered the behavior of thin liquid films on sinusoidally patterned cylinders in two- and three-dimensions using cylindrical coordinates, where the cylinder surface is defined as

$$R(\theta, z) = R_c + \alpha \sin(k_\theta \theta + k_z z). \tag{1.3}$$

Here, R_c is the mean cylinder radius, α is the amplitude of the sinusoidal topography, and k_i are the wavenumbers in the angular (θ) and axial (z) directions. By considering the limit where the topography amplitude α and mean coating thickness are much smaller than R_c, a lubrication-theory-based model was obtained which agreed well with experimental results [25] and with full 2D GFEM simulations for small sinusoidal topography [24]. In the present work, we relax this small-topography assumption and develop a lubrication-theory-based model to study flows on noncircular cylinders with large variations in surface curvature, using elliptical and sinusoidally patterned cylinders as examples.

In §2 we present a lubrication-theory-based model describing the flow of a thin coating on a 2D cylinder whose variations in the radius of curvature are comparable to the cylinder's characteristic radius, in effect relaxing the small-topography assumption [24, 25]. A comparison of results from this large-curvature model to results from the small-topography model [24, 25] and GFEM simulations is presented in §3 to highlight the strengths and limitations of our approach. The large-curvature model is then used to probe the behavior of thin coatings on elliptical cylinders in §4, and conclusions are provided in §5.

2. Mathematical Model

We consider the flow of a Newtonian liquid with constant density ρ, viscosity μ, and surface tension σ on a noncircular cylinder with characteristic radius R_c. The cylinder rotates counterclockwise about its axis at angular speed Ω, and we define the problem using cylindrical coordinates (r, θ, z) with basis vectors $(\boldsymbol{e_r}, \boldsymbol{e_\theta}, \boldsymbol{e_z})$ in a reference frame rotating counterclockwise with the cylinder ($\boldsymbol{\Omega} = \Omega \boldsymbol{e_z}$). The cylinder surface $R(\theta, z)$ is described as a function of the angular and axial

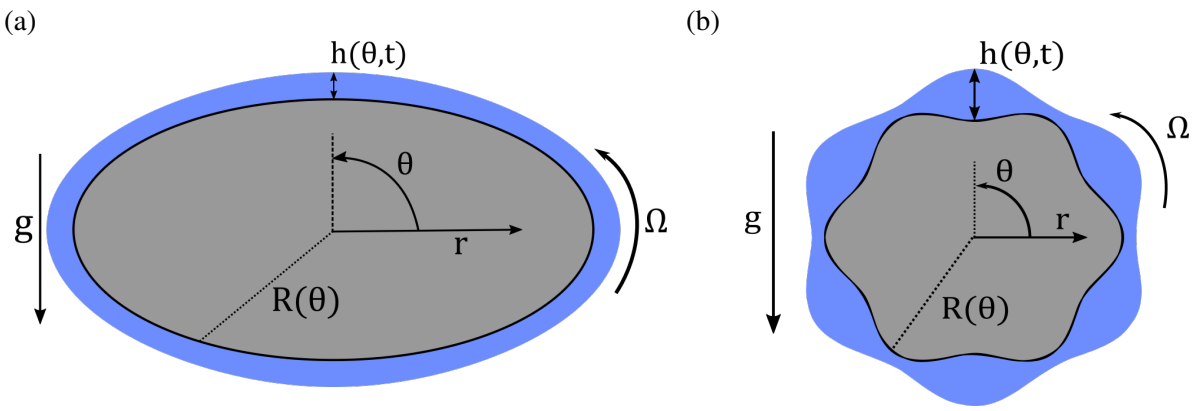

FIG. 1. Model geometries for two noncircular cylinders. **a)** Elliptical cylinder with radius a along the major axis and b along the minor axis. **b)** Sinusoidally patterned cylinder with mean radius R_c and topography given by $R(\theta, z) - R_c$.

coordinates, and the thickness of the liquid film $h(\theta, z, t)$ is defined with respect to the cylinder surface as shown in Fig. 1.

Although the equations we derive are for general shapes, we will present results using elliptical cylinders (Fig. 1a) and sinusoidally patterned cylinders (Fig. 1b). For convenience, a new radial coordinate $y = r - R(\theta, z)$ is defined such that $0 \leq y \leq h(\theta, z, t)$. The position vector $\boldsymbol{r}$ and the liquid velocity $\boldsymbol{u}$ are defined as

$$\boldsymbol{r} = (y + R(\theta, z))\, \boldsymbol{e_r} + z\boldsymbol{e_z}, \tag{2.1}$$

$$\boldsymbol{u} = u_r \boldsymbol{e_r} + u_\theta \boldsymbol{e_\theta} + u_z \boldsymbol{e_z}. \tag{2.2}$$

Note that there is no θ-component of the position vector in cylindrical coordinates. Due to our definition of the the film thickness $h(\theta, z, t)$ and cylinder radius $R(\theta, z)$, each quantity possesses a single value for a given coordinate pair θ and z.

Prior work has examined flow on sinusoidally patterned cylinders in the limit that the topography amplitude is much smaller than the characteristic radius R_c of the cylinder [16, 25]. In the present work, we relax this small-topography assumption and consider flow on a noncircular cylinder where lateral variations in the cylinder radius are comparable to, instead of smaller than, the characteristic radius R_c. A scaling of the governing equations and boundary conditions different from that in Refs. [16, 25] is used to obtain an evolution equation for flow on noncircular cylinders

with large variations in the radius. Details of this approach are provided in §2.2 and Appendix A, while the noncircular cylinders we consider are described in more detail in §2.3.

2.1. Governing Equations and Boundary Conditions

It is convenient to express the governing equations in a reference frame rotating counter-clockwise with the cylinder ($\boldsymbol{\Omega} = \Omega \boldsymbol{e_z}$). In the rotating reference frame, mass and momentum conservation for a Newtonian liquid of density ρ and viscosity μ are

$$\boldsymbol{\nabla} \cdot \boldsymbol{u} = 0, \tag{2.3}$$

$$\rho \left(\frac{\partial \boldsymbol{u}}{\partial t} + \boldsymbol{u} \cdot \boldsymbol{\nabla} \boldsymbol{u} \right) = -\boldsymbol{\nabla} p + \mu \nabla^2 \boldsymbol{u} + \rho \boldsymbol{g} - \rho \boldsymbol{\Omega} \times (\boldsymbol{\Omega} \times \boldsymbol{r}) + 2\rho \boldsymbol{\Omega} \times \boldsymbol{u}, \tag{2.4}$$

where $\boldsymbol{g} = -g \sin(\theta + \Omega t) \boldsymbol{e_r} - g \cos(\theta + \Omega t) \boldsymbol{e_\theta}$ is the gravitational acceleration and p is the liquid pressure. On the cylinder surface, we apply no-penetration and no-slip conditions,

$$\boldsymbol{n_c} \cdot \boldsymbol{u} = 0, \tag{2.5}$$

$$\boldsymbol{t_{c,i}} \cdot \boldsymbol{u} = 0 \qquad (i = \theta, z), \tag{2.6}$$

where $\boldsymbol{n_c}$ and $\boldsymbol{t_{c,i}}$ are the unit vectors normal and tangential to the cylinder surface (Appendix A). At the liquid-air interface, we apply interfacial balances for total mass, normal stress, and tangential stress [26–28],

$$\left(\boldsymbol{u}^l - \boldsymbol{u}^I \right) \cdot \boldsymbol{n} = 0, \tag{2.7}$$

$$p^l - \left[\boldsymbol{n} \cdot \boldsymbol{\tau} \cdot \boldsymbol{n} \right]^l - p^v + \left[\boldsymbol{n} \cdot \boldsymbol{\tau} \cdot \boldsymbol{n} \right]^v = \sigma \boldsymbol{\nabla} \cdot \boldsymbol{n}, \tag{2.8}$$

$$- \left[\boldsymbol{n} \cdot \boldsymbol{\tau} \cdot \boldsymbol{t}_i \right]^l + \left[\boldsymbol{n} \cdot \boldsymbol{\tau} \cdot \boldsymbol{t}_i \right]^v = -\boldsymbol{\nabla}_s \sigma \cdot \boldsymbol{t_i} \, (i = \theta, z) \,, \tag{2.9}$$

where the superscripts l, v, and I respectively denote liquid, vapor, and interface quantities. The scalar σ is the surface tension of the liquid and $\boldsymbol{\tau}$ is the viscous stress tensor (Appendix A). The vectors $\boldsymbol{n}$ and $\boldsymbol{t_i}$ are the outward unit normal and tangent vectors of the liquid-air interface (Appendix A).

2.2. Scaling and Evolution Equation

In many applications of interest, the characteristic thickness H of the liquid film is much smaller than the characteristic cylinder radius R_c, and a small dimensionless characteristic thick-

ness $\epsilon = H/R_c \ll 1$ may be defined. We introduce the following dimensionless quantities, denoted by tildes [10, 16, 25, 29],

$$\begin{gathered}(y,h) = H(\tilde{y},\tilde{h}) \qquad (r,z,R) = R_c(\tilde{r},\tilde{z},\tilde{R}) \qquad t = \Upsilon\tilde{t} \\ u = U\tilde{u} \qquad v = U\tilde{v} \qquad w = U\tilde{w} \qquad p = P\tilde{p}.\end{gathered} \tag{2.10}$$

The characteristic speed $U = \rho g H^2/\mu$, characteristic pressure $P = \mu U/\epsilon H$, and characteristic time $\Upsilon = R_c/U$ are based on gravitational drainage of the coating. The scaling for the axial coordinate z is motivated by prior work [10, 11, 16, 25, 29]. Order-of-magnitude estimates for select dimensional quantities in Eqn. (2.10) are listed in Table 1. Hereafter, we drop the tilde notation from dimensionless variables.

There are two key differences between the scaling in the present work and that of prior work. First, in prior work examining flows on sinusoidally patterned cylinders, the cylinder radius was decomposed into its mean value and a small-amplitude topography, shown in dimensional form in Eqn. (1.3). When the topography amplitude is small—of $\mathcal{O}(\epsilon)$—the effects of surface-tension and centrifugal forces are relegated to $\mathcal{O}(\epsilon)$ terms in the evolution equation [16, 25]. In the present work, we forgo the assumption that variations in the cylinder radius are of $\mathcal{O}(\epsilon)$, and we leave the cylinder radius as an unspecified function of the angular coordinate $R(\theta)$. As a result, the effects of surface-tension and centrifugal forces are retained at leading order.

Second, the scalings for the pressure p and for the radial velocity u in Eqn. (2.10) are different than those used in prior work [10, 11, 16, 25, 29], and they represent more appropriate scalings when variations in the cylinder radius are large compared to the characteristic film thickness H. The pressure and radial velocity scalings are respectively motivated by the normal-stress balance at the liquid-air interface and by mass conservation in the liquid.

Physical interpretations of the pressure and radial velocity scalings are provided here. In the present work, the characteristic pressure $P = \mu U/\epsilon H = \rho g R_c$ is based on drainage of a liquid film from a vertical substrate of length R_c, whereas prior work scaled the pressure as $P = \rho g H$ [10, 11, 16, 29]. Additionally, the radial velocity is scaled with the characteristic velocity U as opposed to ϵU. On noncircular cylinders with large radius variations, liquid may flow radially outward along the cylinder surface at a rate comparable to rate at which liquid would drain due to

Table 1 *Typical dimensional values*

Constant	Order of Magnitude
Viscosity, μ (P)	1
Density, ρ (g cm^{-3})	1
Surface tension, σ (dyn cm^{-1})	$10-100$
Characteristic film thickness, H (cm)	10^{-2}
Characteristic cylinder radius R_c (cm)	$1-10$
Cylinder rotation rate, Ω (rad s^{-1})	10

gravity, and a scaling of $\mathcal{O}(\epsilon)$ becomes inappropriate.

The scaled governing equations and boundary conditions provided in §2.1 are simplified using lubrication theory, as described in Appendix A. The velocity and pressure are expanded as regular perturbation series in the dimensionless characteristic film thickness ϵ, and terms of $\mathcal{O}(\epsilon^2)$ and smaller are neglected. In the present work, we are interested in coating behavior on 2D cross sections of noncircular cylinders, so axial variations in the thickness and cylinder surface are neglected. This procedure yields an evolution equation for the film thickness,

$$\begin{aligned}(R+\epsilon h)\frac{\partial h}{\partial t} = &\frac{\partial}{\partial\theta}\left(\frac{h^3}{3\left(1+m_\theta^2\right)^2}\left(m_\theta\left(W^2R-\sin\theta_r\right)-\left(\cos\theta_r+\frac{1}{Bo\,R}\frac{\partial\kappa_0}{\partial\theta}\right)\right)\right)\\ &+\epsilon\frac{\partial}{\partial\theta}\left(\frac{h^3\frac{\partial h}{\partial\theta}}{3R\left(1+m_\theta^2\right)^3}\left(W^2R-\sin\theta_r+m_\theta\left(\cos\theta_r+\frac{1}{Bo\,R}\frac{\partial\kappa_0}{\partial\theta}\right)\right)\right)\\ &-\epsilon\frac{\partial}{\partial\theta}\left(\frac{h^3}{3Bo\left(1+m_\theta^2\right)^2}\frac{1}{R}\frac{\partial\kappa_1}{\partial\theta}\right)\\ &+\epsilon\frac{\partial}{\partial\theta}\left(\frac{h^4}{6R\left(1+m_\theta^2\right)^3}\left(3+8m_\theta^2-3\frac{1}{R}\frac{\partial^2R}{\partial\theta^2}\right)\left(W^2Rm_\theta-\cos\theta_r\right)\right)\\ &-\epsilon\frac{\partial}{\partial\theta}\left(\frac{h^4}{6R\left(1+m_\theta^2\right)^3}\left(1+6m_\theta^2-3\frac{1}{R}\frac{\partial^2R}{\partial\theta^2}\right)\left(\sin\theta_r+\frac{1}{Bo\,R}\frac{\partial\kappa_0}{\partial\theta}\right)\right).\end{aligned} \tag{2.11}$$

Here, $\theta_r=\theta+MW\epsilon^{-2}t$ gives the orientation of gravity in the rotating reference frame. Quantities m_θ, κ_0, and κ_1 are measures of the cylinder and free-surface curvatures,

$$m_\theta=\frac{1}{R}\frac{\partial R}{\partial\theta}, \tag{2.12}$$

$$\kappa_0=\frac{1}{R\left(1+m_\theta^2\right)^{3/2}}\left(1+m_\theta^2+\frac{1}{R}\frac{\partial^2R}{\partial\theta^2}\right), \tag{2.13}$$

$$\kappa_1 = \frac{\frac{1}{R}\frac{\partial^2 R}{\partial\theta^2}\left(2-m_\theta^2\right)-4m_\theta^2-1}{R^2\left(1+m_\theta^2\right)^{5/2}}h + \frac{m_\theta\left(1-2m_\theta^2+3\frac{1}{R}\frac{\partial^2 R}{\partial\theta^2}\right)}{R^2\left(1+m_\theta^2\right)^{5/2}}\frac{\partial h}{\partial\theta} - \frac{1}{R^2\left(1+m_\theta^2\right)^{3/2}}\frac{\partial^2 h}{\partial\theta^2}. \tag{2.14}$$

Due to the scaling introduced in Eqn. (2.10), inertial forces resulting from gravitational drainage and Coriolis forces are of $\mathcal{O}\left(\epsilon^2\right)$ and neglected through the lubrication approximation. As Eqn. (2.11) describes the flow of a thin liquid coating on noncircular cylinders with large lateral curvature variations (of $\mathcal{O}\left(1\right)$), we refer to it as a large-curvature (LC) model for simplicity. Typical values and physical interpretations of the dimensionless parameters in Eqn. (2.11) are provided in Table 2. Following prior work, we assume that $MW\epsilon^{-2}$, W^2, and Bo^{-1} are of no more than $O(1)$. In practice, W^2 and Bo^{-1} can be much smaller than unity (Table 2). In previous studies using cylinders with small radius variations, this approach has yielded results that agree well with full 2D simulations and with experiments [10, 11, 16, 25, 29].

When variations in the cylinder radius are small compared to the characteristic radius, it is convenient to define the dimensionless cylinder radius as

$$R(\theta) = 1 + \beta B(\theta). \tag{2.15}$$

Here $B(\theta)$ describes the topography of the cylinder and β is a small parameter describing the magnitude of the topography. In the limiting case where $\beta = \mathcal{O}\left(\epsilon\right)$, Eqn. (2.11) may be further simplified via a Taylor-series expansion to yield the evolution equation,

$$\begin{aligned}\left(1+\epsilon h+\beta B\right)\frac{\partial h}{\partial t} = \frac{\partial}{\partial\theta}\left(\cos\theta_r\left(\frac{h^3}{3}+\frac{\epsilon h^4}{2}\right)\right) - \epsilon\frac{\partial}{\partial\theta}\left(\frac{h^3}{3}\left[\left(W^2-\sin\theta_r\right)\frac{\partial}{\partial\theta}\left(h+\frac{\beta}{\epsilon}B\right)\right.\right.\\ \left.\left.+\frac{1}{Bo}\frac{\partial}{\partial\theta}\left(h+\frac{\beta}{\epsilon}B+\frac{\partial^2}{\partial\theta^2}\left(h+\frac{\beta}{\epsilon}B\right)\right)\right]\right).\end{aligned} \tag{2.16}$$

We note that Eqn. (2.16) may obtained directly from the scaled governing equations using lubrication theory in the limit that the topography $B(\theta)$ is small compared to R_c. For the remainder of the present work, we refer to Eqn. (2.16) as the small-curvature (SC) model for simplicity. Notably, Eqn. (2.16) is physically equivalent to the evolution equation used in Ref. [24], where a different non-dimensionalization was used to study the influence of small-amplitude topography.

As mentioned previously, the main consequence of relaxing the small-topography assumption is that the mathematical description of the cylinder geometry is more accurate, causing various

Table 2 *Dimensionless parameters*

Parameter	Definition	Physical Meaning	Typical Value
M	$\mu/\rho\sqrt{gR_c^3}$	viscous forces/gravitational forces	$\mathcal{O}\left(10^{-2}-10^{-1}\right)$
W	$\Omega/\sqrt{g/R_c}$	centrifugal forces/gravitational forces	$\mathcal{O}\left(10^{-3}-10^{-2}\right)$
Bo	$\rho g R_c^2/\sigma$	gravitational forces/surface-tension forces	$\mathcal{O}\left(10-100\right)$
We	$\rho\Omega^2 R_c^3/\sigma$	centrifugal forces/surface-tension forces	$\mathcal{O}\left(10-100\right)$
$\gamma = 1/MW$	$\rho g R_c/\mu\Omega$	gravitational forces/viscous forces	$\mathcal{O}\left(10^1-10^3\right)$

terms that appear at higher orders in the SC model (Eqn. (2.16)) to be retained at lower orders in the LC model (Eqn. (2.11)). In the LC model (Eqn. (2.11)), the more accurate description of the cylinder geometry causes additional terms corresponding to viscous, gravitational, and centrifugal forces to be retained at leading order and $\mathcal{O}\left(\epsilon\right)$ in the momentum balance. Furthermore, additional terms corresponding to surface-tension forces arise in Eqn. (2.11) due to the normal-stress balance at the liquid-air interface. Analysis of our results (not shown here) indicates that the relative importance of these additional terms depends on the choice of model parameters (Table 2).

A film of constant thickness $h(\theta, t=0)=1$ is used as the initial condition for simulations of Eqns. (2.11) and (2.16). Given this initial condition and a set of dimensionless parameters (Table 2), Eqns. (2.11) and (2.16) may be solved numerically. Second-order centered finite differences are used to approximate spatial derivatives. Time integration is carried out semi-implicitly using backward Euler for $\mathcal{O}\left(\epsilon\right)$ terms resulting from curvature of the free surface (κ_1 and $Bo^{-1}\left(h+h_{\theta\theta}\right)$) and forward Euler for the remaining terms. The spatial domain is discretized using a uniform grid spacing defined as $\Delta\theta = 2\pi/n_\theta$, where n_θ is the number of nodes in the θ direction. To properly resolve the spatial and temporal evolution of the coating, a minimum of $n_\theta = 1200$ grid points are used with a maximum time step of $\Delta t = 10^{-4}$. The resulting equations are solved using the Newton-Raphson method.

2.3. Noncircular Cylinders

The function describing the cylinder radius $R(\theta)$ was left unspecified in the derivation of Eqn. (2.11). We examine coating behavior on two types of noncircular cylinders—elliptical cylinders (Fig. 1a) and sinusoidally patterned cylinders (Fig. 1b)—to demonstrate the strengths and limitations of the LC model. While our main focus in this work is coating behavior on elliptical

cylinders, coating behavior on sinusoidally patterned cylinders has been examined in prior work using the SC model and GFEM simulations, and it provides a useful case study to validate the LC model. The dimensionless radius of sinusoidally patterned cylinders is given by

$$R(\theta) = 1 + \beta \sin\left((k_\theta \theta)\right), \tag{2.17}$$

where β is the topography amplitude and k_θ is the topography wavenumber (Fig. 1b), while the dimensionless radius of elliptical cylinders is given by

$$R(\theta) = \frac{\delta}{\sqrt{(1-(1-\delta^2)\cos^2\theta)}}, \tag{2.18}$$

where $\delta = b/a$ is the ratio of the minor axis to the major axis and the characteristic radius R_c is taken to be the radius of the major axis a (Fig. 1a). Regardless of the cylinder type, the load A of a coating with dimensionless thickness $\epsilon h(\theta, t)$ on a cylinder surface with radius $R(\theta)$ is given by

$$A = \int_0^{2\pi} \left[\left(R(\theta) + \epsilon h(\theta, t)\right)^2 - R(\theta)^2 \right] d\theta. \tag{2.19}$$

2.4. 2D Galerkin Finite-Element Method

To test the accuracy of the LC model, results obtained from Eqn. (2.11) are compared to GFEM simulations of the scaled governing equations and boundary conditions,

$$\boldsymbol{\nabla} \cdot \boldsymbol{u} = 0, \tag{2.20}$$

$$-\boldsymbol{\nabla} p + \nabla^2 \boldsymbol{u} + \boldsymbol{g} - W^2 \boldsymbol{r} = 0, \tag{2.21}$$

where $\boldsymbol{r} = r\boldsymbol{e_r}$ is the position vector in 2D and $\boldsymbol{g} = -g\sin\left(MW\epsilon^{-2}t\right)\boldsymbol{e_x} - g\cos\left(MW\epsilon^{-2}t\right)\boldsymbol{e_y}$ is gravity in a Cartesian reference frame rotating with the cylinder. Inertial effects resulting from gravitational drainage and Coriolis forces have been neglected. A description of the GFEM simulations is provided in Li *et al.* [16, 24], and some details are also given in Appendix B. Computational times vary based on the dimensionless rotation rate W, viscosity M, film thickness ϵ, and form of the cylinder surface $R(\theta)$. Most GFEM simulations in the present work take one to four days per one hundred cylinder revolutions. In contrast, most simulations of the LC model (Eqn. (2.11)) and SC model (Eqn. (2.16)) take a few hours per one thousand cylinder revolutions.

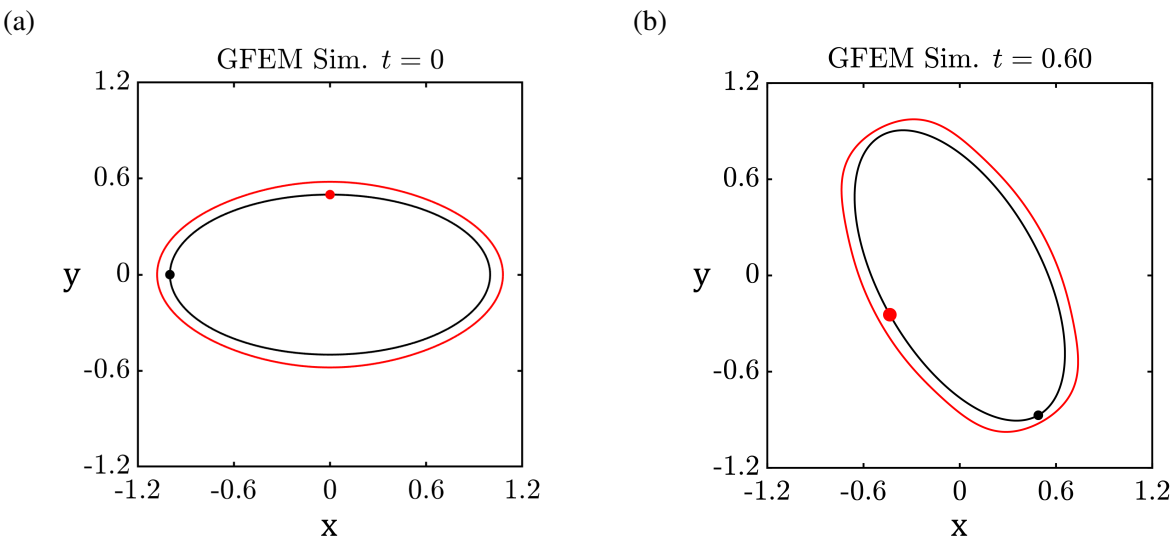

FIG. 2. Coating shapes obtained from GFEM simulations at **a)** $t = 0$ and **b)** $t = 0.6$ for $\epsilon = 0.02$, $M = 0.0958$, $W = 0.67$, $Bo = 12.26$, $\gamma = 15.57$, and $\delta = 0.5$. The coating surface is given in red while the cylinder surface is in black. Red and black dots respectively denote the points $\theta = \pi/2$ and $\theta = \pi$ on the cylinder surface. The coating thickness has been exaggerated by four times to distinguish the coating from the cylinder.

3. Results: Model Validation

To examine the accuracy of the LC model, we compare results obtained with Eqn. (2.11) to results from the SC model (Eqn. (2.16)) and GFEM simulations (§2.4) for flow on elliptical cylinders (Fig. 1a) and sinusoidally patterned cylinders (Fig. 1b).

3.1. Elliptical Cylinders

Simulations have been conducted on elliptical cylinders with aspect ratio $\delta = 0.5$ (Table 2) so that the major axis is twice the length of the minor axis and variations in $R(\theta)$ are large. When variations in $R(\theta)$ are large and the dimensionless characteristic thickness ϵ is small, we expect the LC model to agree well with GFEM simulations. To probe this limit, we examine a representative set of simulation results in Figs. 2–4 for $\epsilon = 0.02$ and $\delta = 0.5$.

In Fig. 2, coating shapes obtained from GFEM simulations on an elliptical cylinder with $\delta = 0.5$ are provided at two times, where the red and black dots in Fig. 2 respectively denote the points $\theta = \pi/2$ and $\theta = \pi$ on the cylinder surface. The initial condition, a coating of uniform thickness, is depicted in Fig. 2a. For the conditions in Fig. 2, surface tension drives liquid away

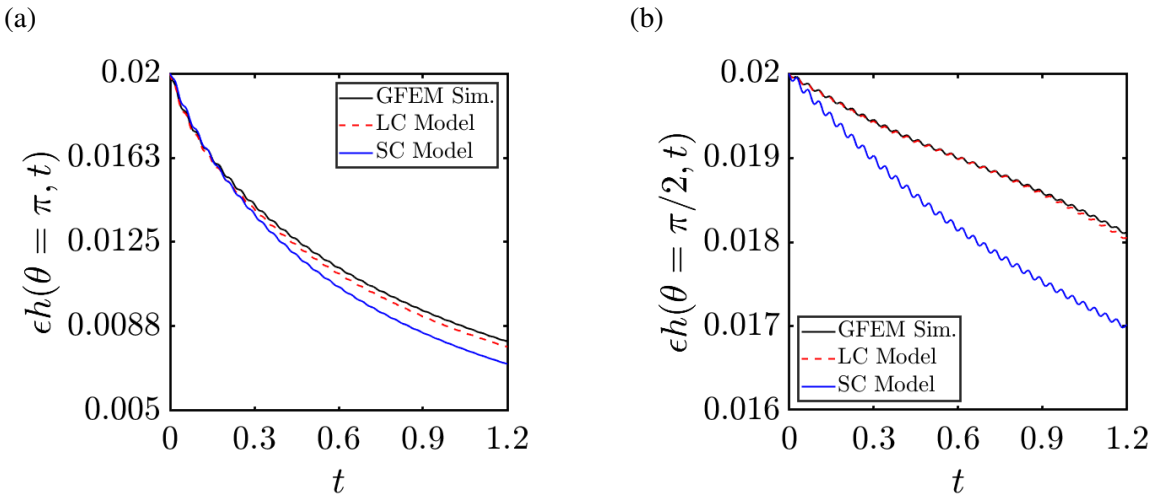

FIG. 3. Film thickness over time at **a)** $\theta = \pi$ and **b)** $\theta = \pi/2$ obtained from GFEM simulations (black line), the LC model (dashed red line), and the SC model (blue line). Model parameters are provided in Fig. 2.

from the tips of the cylinder, leading to a coating which is thinner over the tips (Fig. 2b). The thickest region of the coating is located between the tips and midsection of the cylinder, as can be seen in Fig. 2b.

To demonstrate the utility of the LC model, we compare GFEM results to predictions from Eqn. (2.11) (LC model) and Eqn. (2.16) (SC model). In Fig. 3, the time evolution of the dimensionless film thickness ϵh is provided over points $\theta = \pi$ (Fig. 3a) and $\theta = \pi/2$ (Fig. 3b). Results obtained from the LC model (dashed red lines) are compared to those obtained from GFEM simulations (black lines) and the SC model (blue lines). At both $\theta = \pi$ (Fig. 3a) and $\theta = \pi/2$ (Fig. 3b), the film thickness decreases over time as liquid settles between the midsection and tips of the cylinder, as was highlighted in Fig. 2b. Oscillations in the thicknesses shown in Fig. 3 are the result of gravity, which acts non-uniformly around the cylinder. Additionally, based on the prior work of Hunt, we expect the coating to decay toward a periodic solution whose thickness varies with the orientation of the cylinder [15]. We note that the time evolution of disturbances in thin coatings tends to be inversely proportional to the dimensionless characteristic thickness ϵ, so this decay is expected to be slow for thin coatings like those shown in Fig. 3 [10, 25, 29].

At $\theta = \pi$ (Fig. 3a), the film thickness predicted by the LC model is more accurate than that predicted by the SC model when compared to GFEM simulations. As one might expect,

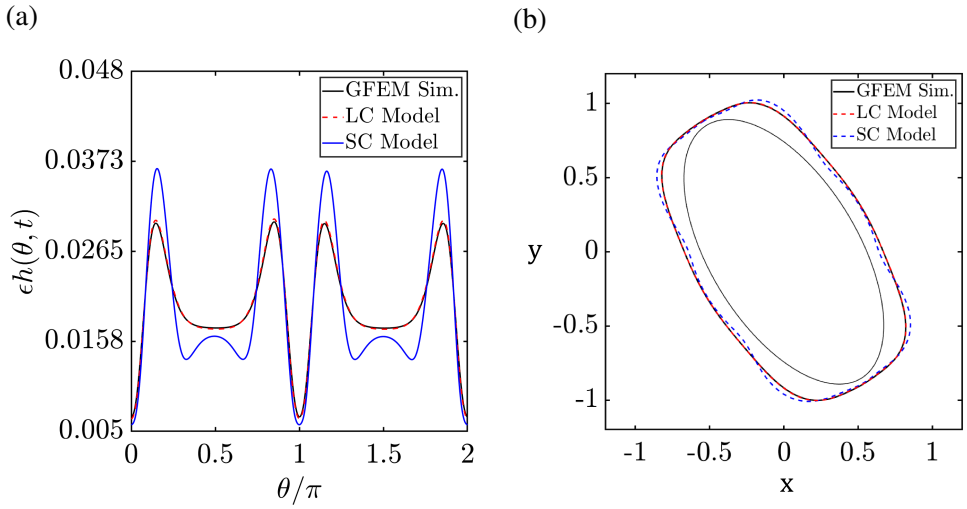

FIG. 4. a) Film thicknesses $\epsilon h(\theta, t)$ at $t = 1.6$ and **b)** coating shapes obtained from the GFEM simulations (thick black line), LC model (dashed red line), and SC model (blue line). The thin black line in **b)** gives the cylinder surface, and the film thickness in **b)** has been exaggerated by six times to highlight thickness variations. Model parameters are provided in Fig. 2.

there is some deviation between the GFEM simulations and the LC model since $\mathcal{O}(\epsilon^2)$ terms have been neglected in Eqn. (2.11). However, this deviation is small for the LC model, roughly 3% at $t = 3000$. In contrast, the deviation between the SC model and GFEM simulations grows from 3% at $t = 750$ to ∼12% at $t = 3000$. At $\theta = \pi/2$ (Fig. 3b), similar observations can be made. The LC model more accurately captures the film thickness at $\theta = \pi/2$, with a deviation of 1% from the GFEM simulations at $t = 3000$, while the SC model underpredicts the film thickness by roughly 6% at $t = 3000$.

In Fig. 4, the entire film thickness functions $\epsilon h(\theta, t)$ (Fig. 4a) are shown at $t = 4000$ with corresponding 2D renderings of the coatings (Fig. 4b). The thickness predicted by the LC model (dashed red line) overlaps with the thickness predicted by the GFEM simulations (black line) while the SC model prediction (blue line) deviates significantly from these (Fig. 4a). Around the midsection of the cylinder ($\theta = \pi/2$ and $\theta = 3\pi/2$), the SC model predicts additional maxima and minima, and these appear as spurious disturbances in the coating shape (Fig. 4b). Additionally, in the thickest regions of the coating, the SC model over-predicts the dimensionless thickness by ∼18% compared to GFEM simulations while the LC model deviates by only 1%. Overall, the LC model agrees well with the GFEM simulations and out-performs the SC model for the case shown in Figs. 2–4.

The results in Figs. 3–4 provide a representative example of the accuracy of the LC model for conditions where good agreement is expected with GFEM simulations—for small dimensionless characteristic thickness ϵ and for variations in $R(\theta)$ which are of $\mathcal{O}(1)$. In Fig. 5, film thicknesses $\epsilon h(\theta, t)$ (Figs. 5a and 5c) and corresponding coating shapes (Figs. 5b and 5d) are shown for higher values of ϵ at fixed aspect ratio $\delta = 0.5$ to demonstrate the effect of ϵ on the accuracy of the LC model. When $\epsilon = 0.045$ (Figs. 5a–5b), the film thickness predicted by the LC model (dashed red line) overlaps with the GFEM simulations (black line), with only a slight deviation ($\sim 1\%$) around $\theta = \pi/2$ and $\theta = \pi$. The film thickness predicted by the SC model (dashed blue line) is less accurate. Similar to what was noted in Fig. 4, additional thickness maxima and minima are predicted by the SC model, and these appear as spurious disturbances in the coating shape (Fig. 5b).

In Figs. 5c–5d, the dimensionless characteristic thickness is increased to $\epsilon = 0.095$, where the coating thickness is large and deviation between the LC model and GFEM simulations is expected to increase. In Fig. 5c, neither the LC model (dashed red line) nor the SC model (dashed blue line) overlaps with the results predicted by the GFEM simulations (black line). While both the LC model and SC model capture key qualitative features of the coating, such as the large peak in thickness near $\theta = 1.25\pi$ and the magnitude of the thickness at a given θ, both models inaccurately predict the presence of some thickness minima and maxima. In Fig. 5d, these spurious disturbances in the coating can be observed for both the LC and SC models. However, the visual agreement between the LC model and GFEM simulations is better. The LC model captures the position of the liquid ridge that hangs on the underside of the cylinder while the SC model poorly predicts its position and predicts spurious disturbances in the shape of the coating within the ridge. Overall, in the results shown in Figs. 2–5, better quantitative agreement with GFEM simulations is obtained over a larger range of dimensionless characteristic thickness ϵ when using the LC model. In addition, in the regime where the LC model is expected to deviate from GFEM simulations, the LC model still captures the correct magnitude of the coating thickness at a given θ, and should still provide useful qualitative information about coating behavior.

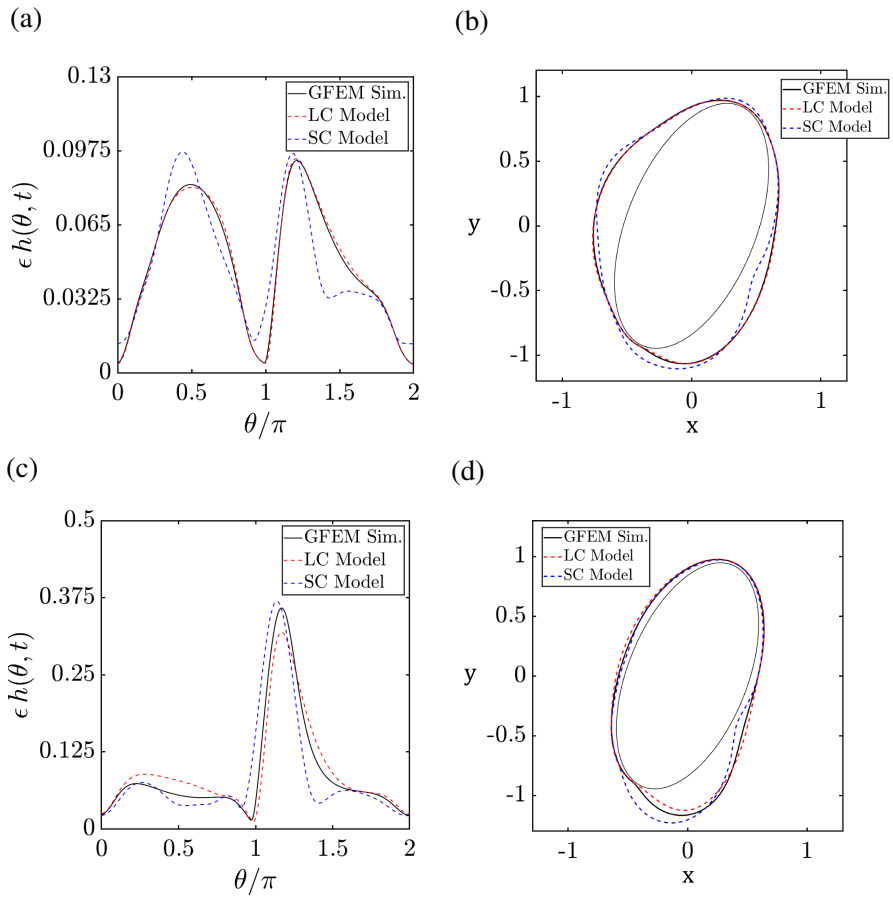

FIG. 5. **a,c)** Film thicknesses and **b,d)** coating shapes obtained from the GFEM simulations (thick black line), LC model (dashed red line), and SC model (dashed blue line). The times are **a,b)** $t = 6.075$ and **c,d)** 27.075. The thin black line in **b,d** gives the cylinder surface. Model parameters are $M = 0.10$, $W = 0.0798$, $Bo = 6$, $\gamma = 125.3$, and $\delta = 0.5$. The dimensionless characteristic thickness is **a,b)** $\epsilon = 0.045$ and **c,d)** $\epsilon = 0.095$. Film thicknesses have been exaggerated by three times in **b)** to highlight thickness variations.

3.2. Sinusoidally Patterned Cylinders with Negligible Gravity

While our main focus is coating behavior on elliptical cylinders, we briefly consider coating behavior on sinusoidally patterned cylinders (Eqn. (2.17)) in the absence of gravity to further validate the LC model (Eqn. (2.11)). The angular topography $B(\theta)$ depends on the topography wavenumber k_θ and the dimensionless topography amplitude β. When the topography $B(\theta)$ is fixed and gravity is neglected in Eqns. (2.11) and (2.16), the Weber number is the key dimensionless parameter controlling coating behavior,

$$We = \frac{\rho \Omega^2 R_c^3}{\sigma}, \tag{3.1}$$

and it describes the ratio of centrifugal to surface-tension forces acting on the coating. In the limit where the topography and film thickness are small, of $\mathcal{O}(\epsilon)$, coating behavior on sinusoidally patterned cylinders has been explored extensively in prior work using the SC model (Eqn. (2.16)) [16, 25]. Here, we examine the limit where the pattern amplitude β is of $\mathcal{O}(1)$ and the SC model is expected to deviate from GFEM simulations.

To demonstrate the effect of the dimensionless characteristic thickness ϵ on the accuracy of the LC model, predictions from Eqn. (2.11) (LC model) and Eqn. (2.16) (SC model) are compared to GFEM simulations in Fig. 6 for two values of the ϵ ($\epsilon = 0.01$ in Figs. 6a–6b and $\epsilon = 0.05$ in Figs. 6c–6d). These simulations are conducted for $k_\theta = 4$ and $\beta = 0.3$, where the topography amplitude is 30% of the mean cylinder radius, and a depiction of the cylinder surface is provided by the inset in Fig. 6a. The film thicknesses at a pattern crest (Fig. 6a,6c) at $\theta = \pi/2$ and a pattern trough (Fig. 6b,6d) at $\theta = \pi/4$ are shown for the GFEM simulations (black lines), LC model (dashed red lines), and SC model (dashed blue lines). For the combination of β and ϵ in Figs. 6a–6b, good agreement is expected between the LC model and GFEM simulations, as was shown for elliptical cylinders in Figs. 3 and 4. We note that oscillations in thickness are not present in Fig. 6 as gravitational forces have been neglected for this set of simulations.

Surface-tension forces dominate coating behavior for the case shown in Figs. 6a and 6b, driving liquid away from pattern crests (Fig. 6a) and toward pattern troughs (Fig. 6b) at a rate which slows down over time. Over the pattern crest (Fig. 6a), both the LC model and SC model correctly predict that the film thickness decreases at a rate which slows slightly over time, but the deviation between the LC model and the GFEM simulations is less than that observed for the SC model. Over the pattern trough (Fig. 6b), the LC model accurately predicts the initial rate at which the thickness increases and that this rate slows down over time. Additionally, deviations between the LC model and GFEM simulations remain below 3% between $t = 0$ and $t = 0.16$. In contrast, the SC model significantly underestimates the initial rate of thickness changes and incorrectly predicts that this rate increases over time, in disagreement with both the GFEM simulations and LC model. As a result of these factors, deviation between the SC model and GFEM simulations is largest near $t = 0.05$ ($\sim 23\%$). Similar to what was observed for flows on elliptical cylinders, agreement between the GFEM simulations and LC model, and the disagreement between these

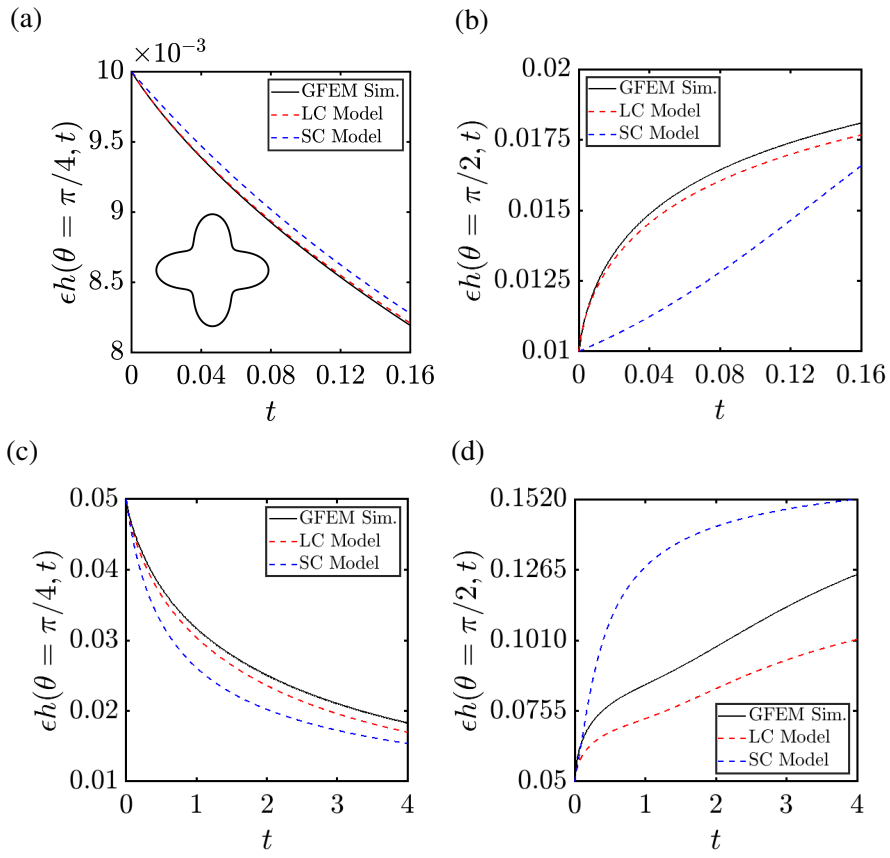

FIG. 6. Film thickness over time for **a,b)** $\epsilon = 0.01$ and **c,d)** $\epsilon = 0.05$ at **a,c)** a pattern trough ($\theta = \pi/4$) and **b,d)** a pattern crest ($\theta = \pi/2$) on a sinusoidally patterned cylinder (Eqn. (2.17)). Model parameters are $\beta = 0.3$, $k_\theta = 4$, and $We = 0.187$. Thicknesses are given for the GFEM simulations (black lines), LC model (dashed red lines), and SC model (dashed blue lines). The inset in **a)** is a depiction of the cylinder surface with $k_\theta = 4$ and $\beta = 0.3$.

and the SC model, is characteristic of simulations for large topography β and small dimensionless characteristic thickness ϵ.

At larger values of ϵ, the asymptotic expansion used to derive the LC model is less accurate and we expect the LC model to deviate from GFEM simulations. In Figs. 6c and 6d, the film thicknesses at a pattern crest $\theta = \pi/2$ (Fig. 6c) and a pattern trough $\theta = \pi/4$ (Fig. 6d) are provided at $\beta = 0.3$ and $\epsilon = 0.05$. Over both the pattern crest and trough, the LC model provides more accurate predictions of the thickness than the SC model when compared to the GFEM simulations. However, at the pattern trough (Fig. 6d), neither the LC model nor the SC model quantitatively agrees with the GFEM simulations, as both deviate from the GFEM simulations by 20% at $t = 4$.

The entire film thickness functions (Fig. 7a) and coating shapes (Fig. 7b) are provided at

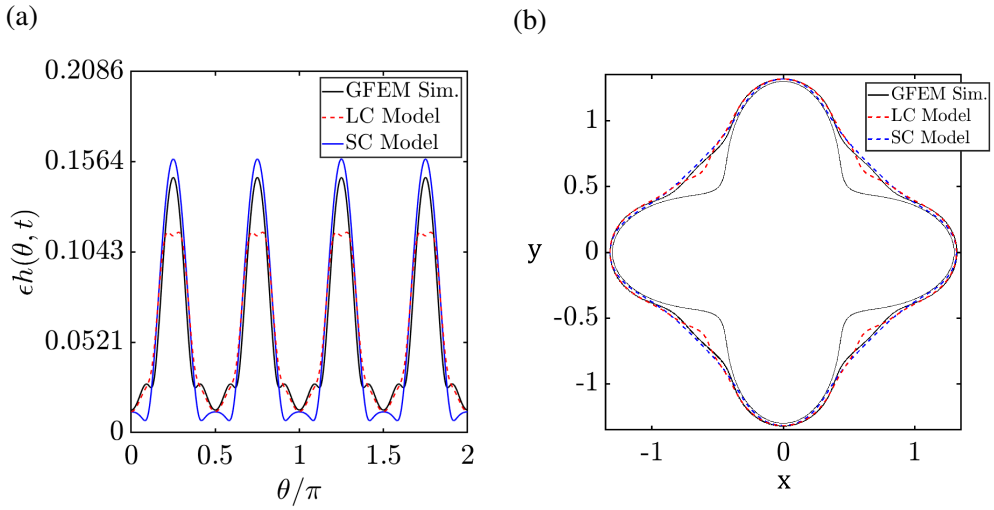

FIG. 7. **a)** Film thicknesses at $t = 4$ and **b)** coating shapes obtained from the GFEM simulations (thick black line), LC model (dashed red line), and SC model (blue line). Model parameters are $\epsilon = 0.05$, $\beta = 0.3$, $k_\theta = 4$, and $We = 0.187$. The thin black line in **b)** gives the cylinder surface, and film thicknesses have been exaggerated by 1.2 times in **b)** to highlight thickness variations.

$t = 4$ in Fig. 7 for the GFEM simulations (black line), LC model (dashed red line), and SC model (dashed blue line). Similar to what was observed on elliptical cylinders, spurious maxima and minima are predicted by the reduced-order models, and they fail to capture some maxima and minima predicted by the GFEM simulations. Also similar to the results from elliptical cylinders, the LC model tends to underpredict the film thickness in thicker regions of the coating, such as for the thickness peaks over pattern troughs ($\theta = n\pi/4$ for odd n). However, the LC model better captures the film thickness in thin regions of the coating ($\theta = n\pi/2$).

4. Results: Elliptical Cylinders

Prior work has examined the behavior of fairly thick coatings ($75 - 80\%$ of the maximum load predicted by Hunt [15]) on rotating elliptical cylinders [15, 16]. In the absence of surface tension, Hunt [15] characterized the effect of the Stokes number γ and cylinder aspect ratio δ on coatings of increasing load A. By gradually increasing the load A, Hunt determined the maximum supportable load A_c^{ellip} above which gravity would cause liquid to drain from the cylinder [15]. Additionally, Hunt found that A_c^{ellip} decreased with increasing Stokes number γ according to the same polynomial expression of γ predicted by Kelmanson [14] for circular cylinders [15]. Li *et al.* extended this work by examining flow on elliptical cylinders in the presence of surface-tension and centrifugal forces using GFEM simulations [16]. While they were able to demonstrate the effects

of load and surface tension on coating behavior, the steep computational cost of GFEM simulations prevented a comprehensive parametric study of coating regimes on elliptical cylinders [16].

The LC model (Eqn. (2.11)) provides a computationally inexpensive alternative to GFEM simulations. In the present work, simulations have been conducted using our LC model (2.11) to provide a comprehensive characterization of coating regimes on elliptical cylinders. Parametric studies of the LC model have been performed for varying load A, Stokes number γ, and Bond number Bo; results are presented for elliptical cylinders with aspect ratios $\delta = 0.5$ and 0.8. Due to the non-uniform cylinder topography and the non-uniform effect of gravity around the cylinder, true steady states may not be encountered, so the results we examine are representative of the quasi-steady behavior of the coating after many revolutions. These quasi-steady states are obtained from initial conditions of uniform film thickness; in general, the quasi-steady states may depend on the shape of the initial coating. We note that since there is no steady base state, a standard linear stability analysis is not feasible for this system.

4.1. Characterization of Regimes

At fixed Stokes number γ and varying load A, four regimes of coating behavior are observed as the load is decreased. The coating transitions from being controlled by gravitational forces at large load to surface-tension forces at small load. In Fig. 8, representative examples of coatings in each regime are shown with Stokes number $\gamma = 20.9$, aspect ratio $\delta = 0.5$, and decreasing load. These figures are characteristic of the quasi-steady coating behavior for each regime. Additionally, the transition between these regimes is gradual, and classification relies on qualitative distinctions in coating behavior motivated by a physical understanding of the problem. For consistency, the coatings in Fig. 8 are shown when the major axis of the cylinder is aligned with gravity. Regime maps exploring the effects of other model parameters are provided in §4.2.

In Fig. 8a, we present a representative example of a coating whose load A is slightly larger than the critical load A_c^{ellip} [15]. When the cylinder's major axis is perpendicular to gravity, (Fig. 8a) a ridge of liquid hangs from the bottom of the upward-moving side of the cylinder. Over a series of revolutions (not shown here), the size and position of the ridge may fluctuate slightly, but the ridge remains on the underside of the cylinder. Below the critical load A_c^{ellip}, gravitational

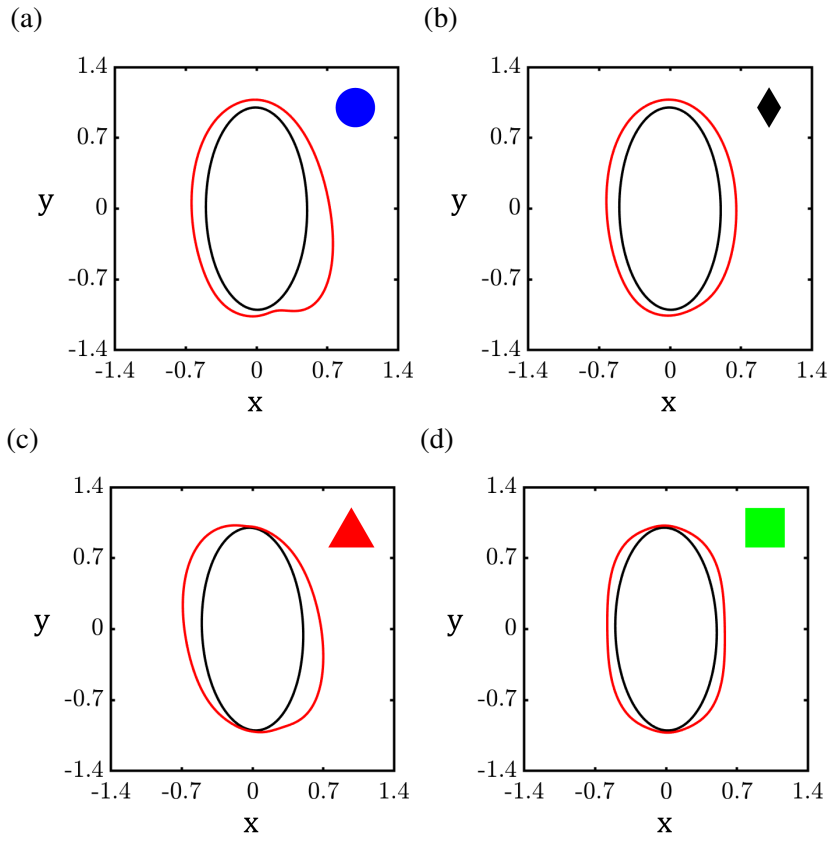

FIG. 8. Coating shapes obtained from the LC model for $M = 0.1$, $W = 0.07982$, $Bo = 12.5$, $\delta = 0.5$, and $\gamma = 20.9$. The loads are **a)** $A = 0.824$, **b)** $A = 0.612$, **c)** $A = 0.3173$, and **d)** $A = 0.1322$ while the critical load predicted by Hunt [15] is $A_c^{ellip} = 0.724$. The coating surface is given in red while the cylinder is in black, and the film thickness has been exaggerated by **c)** three times and **d)** four times to highlight variations in the coating thickness. Inset symbols are provided for reference to the regime maps in §4.1.

forces acting on the coating compete with surface-tension and centrifugal forces to determine coating behavior, leading to the remaining three regimes. In Fig. 8b, the coating shape is shown for a load $A = 0.612$, which is less than $A_c^{ellip} = 0.724$ [15]. Here, the coating is thicker on the upward moving side of the cylinder and thinner on the downward moving side, but there are no visually noticeable disturbances or ridges in the coating like the ridge observed above A_c^{ellip} (Fig. 8a). Over many revolutions, the coating observed in Fig. 8b remains fairly smooth, and thickness disturbances do not develop.

The coatings shown in Figs. 8a and 8b are consistent with those observed in Li *et al.*, where coating behavior was examined near A_c^{ellip} [16]. By continuing to lower the load at $\gamma = 20.9$, two regimes are encountered where surface tension drives the formation of thickness disturbances. In

Fig. 8c, a representative coating is depicted for a load of $A = 0.3173$. Surface tension drives liquid away from the tips of the cylinder, and two ridges of liquid accumulate at opposite ends of the cylinder, with one ridge on the lower-right quadrant of the cylinder and one on upper-left quadrant of the cylinder (Fig. 8c). Over many rotations, these ridges translate with the cylinder and their positions do not vary significantly with the major and minor axes. At early times not shown here, gravity causes liquid to accumulate on the bottom half of the upward moving side of the cylinder, and this contributes to the the asymmetry of the coating seen in Fig. 8c.

At sufficiently low loads, the coating is exceedingly thin, and gravitational forces play a secondary role in coating behavior. In Fig. 8d, we provide a representative coating with load $A = 0.1322$, which is much less than $A_c^{ellip} = 0.724$. Surface tension drives liquid away from the tips of the cylinder and toward the cylinder's midsection. Unlike Fig. 8c, where the coating was asymmetric about the minor axis, the coating in Fig. 8d appears symmetric about the minor axis when the load is sufficiently small. Compared to Fig. 8b, where a visually smooth, asymmetric coating has formed which is slightly thicker on the upward moving side of the cylinder, the coating shown at lower load in Fig. 8d contains four nodules of liquid which are spaced symmetrically about the major and minor axes of the cylinder. Additionally, the coating in Fig. 8d changes little over each cylinder revolution.

4.2. Regime Maps

Fig. 9 provides a regime map exploring the effect of Stokes number γ and load A on coating behavior on an elliptical cylinder at fixed aspect ratio and Bond number ($\delta = 0.5$ and $Bo = 12.5$). We note that the Bond number is the same as that used in the GFEM simulations of Li *et al.* [16]. The blue, black, red, and green symbols denote simulations characteristic of the coatings shown in Figs. 8a–8d respectively, and the black line denotes the critical load A_c^{ellip} predicted by Hunt [15]. Similar to the results of the GFEM simulations in Li *et al.* [16], the LC model predicts that the critical load A_c^{ellip} slightly underestimates the boundary separating the regime where a ridge of liquid hangs on the underside of the cylinder (blue symbols in Fig. 9, Fig. 8a) and the regime where cylinder rotation and surface tension may support the weight of the coating without substantial thinning over the cylinder tips (black symbols in Fig. 9, Fig. 8b).

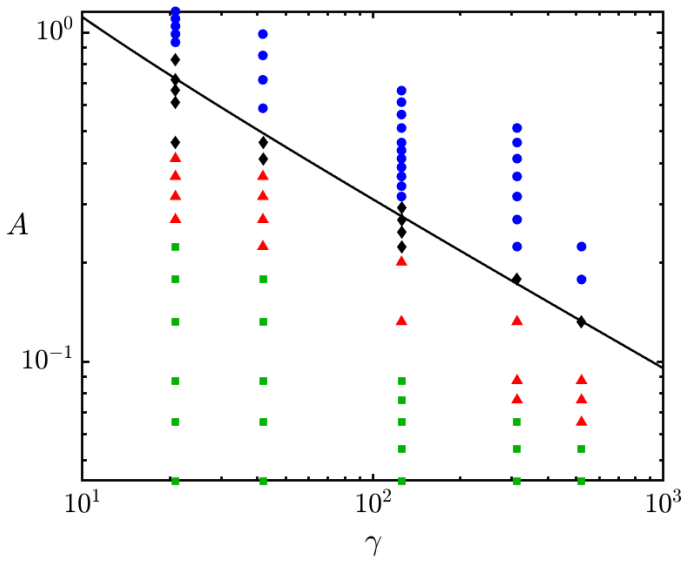

FIG. 9. Regime map obtained from LC model for an elliptical cylinder ($\delta = 0.5$) with varying load A and Stokes number γ. The Bond number is fixed to $Bo = 12.5$. Blue circles, black diamonds, red triangles, and green squares denote coating shapes characterized by Figs. 8a–8d, respectively. The black line is the critical load A_c^{ellip} predicted by Hunt for $\delta = 0.5$ [15].

Decreasing the load below A_c^{ellip} weakens gravitational effects, and surface-tension dominated regimes may be encountered which were not probed by Hunt [15] or Li *et al.* [16]. When the load A is roughly 70% of the critical load A_c^{ellip} predicted by Hunt [15], a regime emerges where surface-tension forces drive liquid away from the cylinder tips into two ridges of liquid located on opposite quadrants of the cylinder (red triangles in Fig. 9, Fig. 8c). For this regime, the load is small enough for surface tension to dominate, but also sufficiently large that gravity gives rise to an asymmetric coating (Fig. 8c).

By lowering the load to roughly 30% of the critical load A_c^{ellip} predicted by Hunt [15], gravitational forces on the coating become negligible, and a regime is encountered where liquid is driven away from the cylinder tips into liquid ridges which are symmetric about the minor axis (green symbols in Fig. 9, Fig. 8d). Practically, the surface-tension-dominated regimes given by the red triangles and green squares in Fig. 9 yield undesirable coatings with larger thickness variations than those given by the black symbols, where surface-tension forces, gravity, and cylinder rotation are balanced (Fig. 8b). As a result, the regime map generated by the LC model (Fig. 9) indicates that the most uniform coatings may be obtained for a limited parameter space just below the crit-

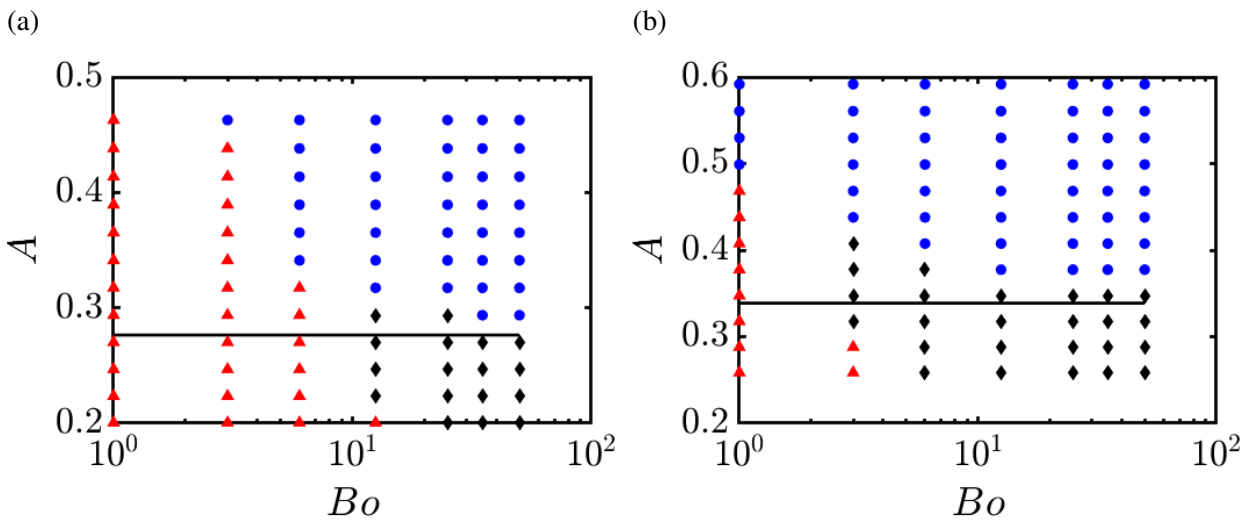

FIG. 10. Regime maps at fixed Stokes number $\gamma = 125.3$ obtained from the LC model on elliptical cylinders with **a)** $\delta = 0.5$ and **b)** $\delta = 0.8$ with varying load A and Bond number Bo. Blue circles, black diamonds, and red triangles denote coating shapes characterized by Figs. 8a–8c, respectively. The black lines are the critical loads A_c^{ellip} predicted by Hunt [15].

ical load predicted by Hunt [15], and that small changes in the load or Stokes number from these desirable conditions may cause the formation of a non-uniform coating.

As the Bond number Bo and aspect ratio δ are changed, the strength of surface-tension forces acting on the coating is expected to change and the regimes observed in Fig. 9 may shift. While this effect was considered briefly in Li *et al.* [16], the LC model provides a means to probe the effect of Bo and δ in more detail for a wider range of parameters. In Fig. 10, we present regime maps of the coating behavior with varying load A and Bond number Bo for two aspect ratios ($\delta = 0.5$ and 0.8) at fixed Stokes number $\gamma = 125.3$. The symbols of various colors correspond to the regimes presented in Figs. 8 and 9, and the black line in Figs. 10a and 10b is the critical load A_c^{ellip} predicted by Hunt [15].

When the aspect ratio is $\delta = 0.5$ (Fig. 10a), capillary-pressure gradients dominate coating behavior at sufficiently low Bond number. At the lowest Bond number in Fig. 10a ($Bo = 1$), asymmetric surface-tension dominated coatings (Fig. 8c) are observed for all loads A regardless of whether the load is less than or greater than the critical load A_c^{ellip} predicted by Hunt [15]. As the Bond number is increased, surface-tension forces become weaker, and gravity acting on the coating becomes more important. At $Bo = 3$, a transition between the asymmetric surface-tension-

dominated regime (Fig. 8c) and gravity-dominated regime (Fig. 8a) occurs above a critical load A, and increasing the Bond number to $Bo = 6$ lowers the load at which this transition occurs.

For sufficiently large Bond number ($Bo \geq 12.5$; Fig. 10a), gravitational effects become strong compared to surface-tension effects, and the coating regimes resemble those probed by Li *et al.* [16] and Hunt [15]. Here, a hanging ridge of liquid is observed when $A > A_c^{ellip}$ (blue circles; Fig. 8a) and a smooth coating thicker on the upward-moving side is observed when $A < A_c^{ellip}$ (black diamonds; Fig. 8b). At moderate Bond number ($Bo = 12.5$), surface-tension forces have a small but measurable effect on the critical load predicted by Hunt [15]. As was observed by Li *et al.* [16], a slightly larger load may be supported by cylinder rotation than this critical load. For relatively large Bo, the critical load A_c^{ellip} of Hunt [15] predicts the boundary between these regimes well, as the dominant balance is between viscous and gravitational forces while surface-tension forces are weak.

When the aspect ratio is increased to $\delta = 0.8$ (Fig. 10b), variations in the cylinder curvature are smaller, and we expect capillary-pressure gradients to play a diminished role in coating behavior. When Bo is small ($Bo = 1$), the asymmetric surface-tension-dominated regime (red triangles; Fig. 8c) is observed at low loads, where gravitational forces are weak, and a transition to the gravity-dominated regime (blue circles; Fig. 8a) may be observed upon increasing the load. While this was was observed at $\delta = 0.5$ in Fig. 10a, the transition between these regimes occurs for smaller loads A and Bond numbers Bo compared to $\delta = 0.8$, as variations in the cylinder curvature are smaller. Upon increasing the Bond number to $Bo = 3$, surface-tension forces become weaker relative to gravitational and viscous forces. As a result, the asymmetric surface-tension dominated regime is only observed at low loads, and increasing the load above $A = 0.3$ first gives rise to the smooth coating observed in Fig. 8b (black diamonds) followed by the gravity-dominated regime (blue circles; Fig. 8a) above $A \approx 0.4$. At $\delta = 0.8$, the smooth-coating regime emerges for lower Bo than at $\delta = 0.5$ as capillary-pressure gradients are weaker for the larger aspect ratio. However, as was observed for $\delta = 0.5$, when the Bond number is increased further ($Bo \geq 6$ in Fig. 10b), surface-tension effects become sufficiently weak that the asymmetric surface-tension dominated regime (Fig. 8c) is not observed in the parameter range we probe. Instead, a hanging ridge may be observed when $A > A_c^{ellip}$ (blue circles; Fig. 8a) while a smooth coating is observed when

$A < A_c^{ellip}$ (black diamonds; Fig. 8b).

Practically, an important application at small Bond number involves the coating of small objects, such as catheters and stents, where the characteristic size of the object (R_c) is comparable to the capillary length ($l_c = \sqrt{\sigma/\rho g}$); catheters necessarily have small diameters ($1 - 2\,$mm) to navigate arteries while the individual struts of stents typically have diameters less than $100\,\mu$m. The investigation undertaken herein, especially the regime maps characterizing the effects of load A and aspect ratio δ at small Bo, probes regimes relevant to these coating processes and it examines effects not captured by Hunt [15], where surface-tension effects were neglected, or Li *et al.*, which focused primarily on coating behavior at large Bo.

5. Conclusions

Liquid flow on the outside of noncircular cylinders is a useful model problem to examine coating behavior on surfaces with nonuniform surface curvature, such as medical devices and endoprostheses. Herein, a lubrication-theory-based model for flow on cylinders with large curvature variations (LC model) is used to examine coating behavior on rotating elliptical cylinders. At small dimensionless characteristic thicknesses, this LC model provides more accurate predictions of the coating thickness than the small-curvature (SC) model of prior work [24, 25] when compared to fully 2D GFEM simulations. As the dimensionless characteristic thickness increases, the LC model becomes less accurate, but it may still capture key qualitative features of coating behavior. Overall, the LC model provides accurate solutions over a larger range of coating thicknesses and cylinder shapes than the SC model.

On elliptical cylinders, the relatively inexpensive computational cost associated with the LC model permits a comprehensive parametric study which is costly to obtain with GFEM simulations [24]. Four regimes of coating behavior are identified which span gravity-dominated (Fig. 8a) to surface-tension-dominated (Fig. 8d). At low loads A and low Bond number Bo, the regime maps in Figs. 9 and 10 provide useful information about coating behavior when surface-tension effects dominate, and this was not examined by Li *et al.*, who focused primarily on moderate Bond number, and Hunt [15], who neglected surface-tension effects. When the Bond number is increased, surface-tension forces become weaker relative to gravitational forces, and the LC model

recovers the behavior observed by Hunt [15] and Li *et al.* [16].

Practically, the parameter space yielding smooth coatings on elliptical cylinders is limited (Figs. 9 and 10), suggesting the need for additional steps to widen this coating window. For example, prior work has demonstrated that surfactants may be used to slow down the growth rate of thickness disturbances in coatings on rotating circular cylinders by introducing Marangoni stresses which drive liquid toward thinner regions of the coating [30]. In the present problem, Marangoni stresses produced by surfactants may reduce the thickness variations produced by capillary-pressure gradients and thereby widen the window in which smooth coatings are attainable.

Acknowledgments

We thank the Industrial Partnership for Research in Interfacial and Materials Engineering of the University of Minnesota and PPG Industries, Inc. for their support. This material is based upon work also supported in part by the National Science Foundation under Grant No. CMMI-2100765. We are grateful to the Minnesota Supercomputing Institute (MSI) at the University of Minnesota for providing computational resources for this research.

The authors report no conflicts of interest.

Appendix A Derivation of Lubrication-Theory-Based Model

Here, we derive the evolution equation for large curvature (Eqn. (2.11)). After rescaling using (2.10)) the governing equations (2.3) and (2.4) become

$$\frac{\partial}{\partial y}(ru) - \frac{\partial R}{\partial \theta}\frac{\partial v}{\partial y} - r\frac{\partial R}{\partial z}\frac{\partial w}{\partial y} + \epsilon\left(\frac{\partial v}{\partial \theta} + r\frac{\partial w}{\partial z}\right) = 0, \tag{A.1}$$

$$\begin{aligned}
&\frac{\epsilon^5(R+\epsilon y)^2}{M^2}\left(\frac{\partial u}{\partial t} + \frac{u}{\epsilon}\frac{\partial u}{\partial y} + \frac{v}{R+\epsilon y}\left(\frac{\partial u}{\partial \theta} - \frac{1}{\epsilon}\frac{\partial R}{\partial \theta}\frac{\partial u}{\partial y}\right) - \frac{v^2}{R+\epsilon y} + w\left(\frac{\partial u}{\partial z} - \frac{1}{\epsilon}\frac{\partial R}{\partial z}\frac{\partial u}{\partial y}\right)\right)\\
&= \epsilon(R+\epsilon y)^2\left(g_r + W^2(R+\epsilon y)\right) - (R+\epsilon y)^2\frac{\partial p}{\partial y} + \epsilon\left[(R+\epsilon y)^2\frac{\partial^2 u}{\partial y^2} - \epsilon^2 u + \epsilon(R+\epsilon y)\frac{\partial u}{\partial y}\right.\\
&\qquad + \epsilon^2\left(\frac{\partial^2 u}{\partial \theta^2} - \frac{1}{\epsilon}\frac{\partial}{\partial \theta}\left(\frac{\partial R}{\partial \theta}\frac{\partial u}{\partial y}\right) - \frac{1}{\epsilon}\frac{\partial R}{\partial \theta}\frac{\partial}{\partial y}\frac{\partial u}{\partial \theta} + \frac{1}{\epsilon^2}\left(\frac{\partial R}{\partial \theta}\right)^2\frac{\partial^2 u}{\partial y^2}\right)\\
&\qquad \left.\epsilon^2\left(\frac{\partial^2 u}{\partial z^2} - \frac{1}{\epsilon}\frac{\partial}{\partial z}\left(\frac{\partial R}{\partial z}\frac{\partial u}{\partial y}\right) - \frac{1}{\epsilon}\frac{\partial R}{\partial z}\frac{\partial}{\partial y}\frac{\partial u}{\partial z} + \frac{1}{\epsilon^2}\left(\frac{\partial R}{\partial z}\right)^2\frac{\partial^2 u}{\partial y^2}\right) - 2\epsilon^2\left(\frac{\partial v}{\partial \theta} - \frac{\partial R}{\partial \theta}\frac{\partial v}{\partial y}\right)\right],
\end{aligned} \tag{A.2}$$

$$\begin{aligned}
&\frac{\epsilon^5(R+\epsilon y)^2}{M^2}\left(\frac{\partial v}{\partial t} + \frac{u}{\epsilon}\frac{\partial v}{\partial y} + \frac{v}{R+\epsilon y}\left(\frac{\partial v}{\partial \theta} - \frac{1}{\epsilon}\frac{\partial R}{\partial \theta}\frac{\partial v}{\partial y}\right) + \frac{uv}{R+\epsilon y} + w\left(\frac{\partial v}{\partial z} - \frac{1}{\epsilon}\frac{\partial R}{\partial z}\frac{\partial v}{\partial y}\right)\right)\\
&= \epsilon(R+\epsilon y)^2 g_\theta - \epsilon(R+\epsilon y)\left(\frac{\partial p}{\partial \theta} - \frac{1}{\epsilon}\frac{\partial R}{\partial \theta}\frac{\partial p}{\partial y}\right) + \epsilon\left[(R+\epsilon y)^2\frac{\partial^2 v}{\partial y^2} - \epsilon^2 v + \epsilon(R+\epsilon y)\frac{\partial v}{\partial y}\right.\\
&\qquad + \epsilon^2\left(\frac{\partial^2 v}{\partial \theta^2} - \frac{1}{\epsilon}\frac{\partial}{\partial \theta}\left(\frac{\partial R}{\partial \theta}\frac{\partial v}{\partial y}\right) - \frac{1}{\epsilon}\frac{\partial R}{\partial \theta}\frac{\partial}{\partial y}\frac{\partial v}{\partial \theta} + \frac{1}{\epsilon^2}\left(\frac{\partial R}{\partial \theta}\right)^2\frac{\partial^2 v}{\partial y^2}\right)\\
&\qquad \left.\epsilon^2\left(\frac{\partial^2 v}{\partial z^2} - \frac{1}{\epsilon}\frac{\partial}{\partial z}\left(\frac{\partial R}{\partial z}\frac{\partial v}{\partial y}\right) - \frac{1}{\epsilon}\frac{\partial R}{\partial z}\frac{\partial}{\partial y}\frac{\partial v}{\partial z} + \frac{1}{\epsilon^2}\left(\frac{\partial R}{\partial z}\right)^2\frac{\partial^2 v}{\partial y^2}\right) + 2\epsilon^2\left(\frac{\partial u}{\partial \theta} - \frac{\partial R}{\partial \theta}\frac{\partial u}{\partial y}\right)\right],
\end{aligned} \tag{A.3}$$

$$\begin{aligned}
&\frac{\epsilon^5(R+\epsilon y)^2}{M^2}\left(\frac{\partial w}{\partial t} + \frac{u}{\epsilon}\frac{\partial w}{\partial y} + \frac{v}{R+\epsilon y}\left(\frac{\partial w}{\partial \theta} - \frac{1}{\epsilon}\frac{\partial R}{\partial \theta}\frac{\partial w}{\partial y}\right) + w\left(\frac{\partial w}{\partial z} - \frac{1}{\epsilon}\frac{\partial R}{\partial z}\frac{\partial w}{\partial y}\right)\right)\\
&= -\epsilon(R+\epsilon y)^2\left(\frac{\partial p}{\partial z} - \frac{1}{\epsilon}\frac{\partial R}{\partial z}\frac{\partial p}{\partial y}\right) + \epsilon\left[(R+\epsilon y)^2\frac{\partial^2 w}{\partial y^2} + \epsilon(R+\epsilon y)\frac{\partial w}{\partial y}\right.\\
&\qquad + \epsilon^2\left(\frac{\partial^2 w}{\partial \theta^2} - \frac{1}{\epsilon}\frac{\partial}{\partial \theta}\left(\frac{\partial R}{\partial \theta}\frac{\partial w}{\partial y}\right) - \frac{1}{\epsilon}\frac{\partial R}{\partial \theta}\frac{\partial}{\partial y}\frac{\partial w}{\partial \theta} + \frac{1}{\epsilon^2}\left(\frac{\partial R}{\partial \theta}\right)^2\frac{\partial^2 w}{\partial y^2}\right)\\
&\qquad \left.\epsilon^2\left(\frac{\partial^2 w}{\partial z^2} - \frac{1}{\epsilon}\frac{\partial}{\partial z}\left(\frac{\partial R}{\partial z}\frac{\partial w}{\partial y}\right) - \frac{1}{\epsilon}\frac{\partial R}{\partial z}\frac{\partial}{\partial y}\frac{\partial w}{\partial z} + \frac{1}{\epsilon^2}\left(\frac{\partial R}{\partial z}\right)^2\frac{\partial^2 w}{\partial y^2}\right)\right].
\end{aligned} \tag{A.4}$$

No slip (2.5) and no penetration (2.6) at the cylinder surface ($y = 0$) are

$$u = v = w = 0. \tag{A.5}$$

The tangential-stress balance (2.9) at the liquid-air interface ($y = h$) is

$$[\boldsymbol{n} \cdot \boldsymbol{\tau} \cdot \boldsymbol{t_\theta}] = 0, \tag{A.6}$$

$$[\boldsymbol{n} \cdot \boldsymbol{\tau} \cdot \boldsymbol{t_z}] = 0. \tag{A.7}$$

The vectors $\boldsymbol{n}$ and $\boldsymbol{t_i}$ are the unit outward normal and tangent vectors of the liquid-air interface, defined as

$$\boldsymbol{n} = \frac{1}{N^{1/2}} \left(\boldsymbol{e_r} - \frac{1}{r} \left(\frac{\partial (h+R)}{\partial \theta} \right) \boldsymbol{e_\theta} - \left(\frac{\partial (h+R)}{\partial z} \right) \boldsymbol{e_z} \right), \tag{A.8}$$

$$\boldsymbol{t}_\theta = \left[\frac{1}{r} \frac{\partial (h+R)}{\partial \theta} \boldsymbol{e_r} + \boldsymbol{e_\theta} \right] \left(1 + \left(\frac{1}{r} \frac{\partial (h+R)}{\partial \theta} \right)^2 \right)^{-1/2}, \tag{A.9}$$

$$\boldsymbol{t}_z = \left[\frac{\partial (h+R)}{\partial z} \boldsymbol{e_r} + \boldsymbol{e_z} \right] \left(1 + \left(\frac{\partial (h+R)}{\partial z} \right)^2 \right)^{-1/2}, \tag{A.10}$$

where

$$N = 1 + \left(\frac{1}{r} \frac{\partial (h+R)}{\partial \theta} \right)^2 + \left(\frac{\partial (h+R)}{\partial z} \right)^2. \tag{A.11}$$

The normal stress balance is

$$p - \epsilon \boldsymbol{n} \cdot \boldsymbol{\tau} \cdot \boldsymbol{n} = \frac{1}{Bo} \kappa, \tag{A.12}$$

where the free-surface curvature is $\kappa = \boldsymbol{\nabla} \cdot \boldsymbol{n}$. The viscous stress tensor is given by $\boldsymbol{\tau} = 2\mu \boldsymbol{D}$, where μ is the liquid viscosity and the components of $\boldsymbol{D}$ are

$$D_{yy} = \frac{\partial u}{\partial y} \tag{A.13}$$

$$D_{\theta\theta} = \frac{1}{R + \epsilon y} \left(\epsilon \frac{\partial v}{\partial \theta} - \frac{\partial R}{\partial \theta} \frac{\partial v}{\partial y} \right) \tag{A.14}$$

$$D_{zz} = \epsilon \frac{\partial w}{\partial z} - \frac{\partial R}{\partial z} \frac{\partial w}{\partial y} \tag{A.15}$$

$$2D_{y\theta} = 2D_{\theta y} = r \frac{\partial}{\partial y} \left(\frac{v}{r} \right) + \frac{\epsilon}{r} \left(\frac{\partial u}{\partial \theta} - \frac{1}{\epsilon} \frac{\partial R}{\partial \theta} \frac{\partial u}{\partial y} \right) \tag{A.16}$$

$$2D_{yz} = 2D_{zy} = \frac{\partial w}{\partial y} + \epsilon \frac{\partial u}{\partial z} - \frac{\partial R}{\partial z} \frac{\partial u}{\partial y} \tag{A.17}$$

$$2D_{z\theta} = 2D_{\theta z} = \epsilon\frac{\partial v}{\partial z} - \frac{\partial R}{\partial z}\frac{\partial v}{\partial y} + \frac{1}{R+\epsilon y}\left(\epsilon\frac{\partial w}{\partial \theta} - \frac{\partial R}{\partial \theta}\frac{\partial w}{\partial y}\right). \tag{A.18}$$

A.1 Perturbation Series Expansion

Following Refs. [10] and [11], we expand the velocities, pressure, and curvature in powers of the small parameter ϵ as

$$u = u^{(0)} + \epsilon u^{(1)} + \dots, \tag{A.19}$$

$$v = v^{(0)} + \epsilon v^{(1)} + \dots, \tag{A.20}$$

$$w = w^{(0)} + \epsilon w^{(1)} + \dots, \tag{A.21}$$

$$p = p^{(0)} + \epsilon p^{(1)} + \epsilon^2 p^{(2)} \dots, \tag{A.22}$$

$$\kappa = \kappa^{(0)} + \epsilon\kappa^{(1)} + \dots. \tag{A.23}$$

Note that in prior work, a constant term $p_0 = Bo^{-1}$ appears at $\mathcal{O}(\epsilon^{-1})$ to account for the pressure change for a film that conforms to the shape of a cylinder with mean curvature of $1/R_c$ [10, 11, 16, 25, 29]. Here, since the pressure is scaled with $P\ \mu U/\epsilon H$ and the topography is assumed to be large, the effect of the cylinder curvature arises at leading order ($p^{(0)}$) and it is no longer constant, as will be shown.

The curvature κ at each order is obtained via a Taylor-series expansion of $\boldsymbol{\nabla}\cdot\boldsymbol{n}$ in terms of ϵ near $\epsilon = 0$. To solve for the pressure and velocity at each order, we substitute Eqns. (A.19)–(A.22) into the governing equations (A.1)–(A.4) and boundary conditions (A.6)–(A.12). Mathematica is used to solve the system of differential equations resulting from this perturbation expansion.

At $\mathcal{O}(1)$, the leading-order differential equation for the pressure is

$$\frac{\partial p^{(0)}}{\partial y} = 0. \tag{A.24}$$

Applying the normal-stress balance at $y = h$

$$p^{(0)}(y = h) = \frac{\kappa^{(0)}}{Bo}, \tag{A.25}$$

yields

$$p^{(0)} = \frac{\kappa^{(0)}}{Bo}. \tag{A.26}$$

At $\mathcal{O}(\epsilon)$ for the pressure and $\mathcal{O}(1)$ for the velocities, we solve a system of differential equations

$$\frac{\partial u^{(0)}}{\partial y} = m_\theta \frac{\partial v^{(0)}}{\partial y} + m_z \frac{\partial w^{(0)}}{\partial y}, \tag{A.27}$$

$$\frac{\partial p^{(1)}}{\partial y} = W^2 R - \sin\theta_r - \frac{2y}{R}\frac{\partial p^{(0)}}{\partial y} + \left(1 + m_\theta^2 + m_z^2\right)\frac{\partial^2 u_0}{\partial y^2}, \tag{A.28}$$

$$\left(1 + m_\theta^2 + m_z^2\right)\frac{\partial^2 v^{(0)}}{\partial y^2} = -m_\theta \frac{\partial p^{(1)}}{\partial y} - \frac{y\, m_\theta}{R}\frac{\partial p^{(0)}}{\partial y} + \frac{1}{R}\frac{\partial p^{(0)}}{\partial \theta} + \cos\theta_r, \tag{A.29}$$

$$\left(1 + m_\theta^2 + m_z^2\right)\frac{\partial^2 w^{(0)}}{\partial y^2} = -m_z \frac{\partial p^{(1)}}{\partial y} - \frac{2y\, m_z}{R}\frac{\partial p^{(0)}}{\partial y} + \frac{\partial p^{(0)}}{\partial z}, \tag{A.30}$$

where

$$m_\theta = \frac{1}{R}\frac{\partial R}{\partial \theta} \qquad m_z = \frac{\partial R}{\partial z}. \tag{A.31}$$

Integrating through the depth y and applying boundary conditions yields

$$u^{(0)} = m_\theta\, v^{(0)} + m_z\, w^{(0)}, \tag{A.32}$$

$$\begin{aligned} v^{(0)} = \frac{y^2/2 - yh}{\left(1 + m_\theta^2 + m_z^2\right)^2} \Bigg(& \left(1 + m_z^2\right)\cos\theta_r - m_\theta\, sin\theta_r - W^2 R\, m_\theta \\ & + \frac{1 + m_z^2}{R\, Bo}\frac{\partial \kappa^{(0)}}{\partial \theta} - \frac{m_\theta m_z}{Bo}\frac{\partial \kappa^{(0)}}{\partial z}\Bigg), \end{aligned} \tag{A.33}$$

$$\begin{aligned} w^{(0)} = \frac{y^2/2 - yh}{\left(1 + m_\theta^2 + m_z^2\right)^2} \Bigg(& m_z\, \sin\theta_r - W^2 R\, m_z - m_z m_\theta \cos\theta_r \\ & + \frac{1 + m_\theta^2}{R\, Bo}\frac{\partial \kappa^{(0)}}{\partial z} - \frac{m_\theta m_z}{RBo}\frac{\partial \kappa^{(0)}}{\partial \theta}\Bigg), \end{aligned} \tag{A.34}$$

$$\begin{aligned} p^{(1)} = \frac{y - h}{\left(1 + m_\theta^2 + m_z^2\right)^2} \Bigg(& W^2 R - \sin\theta_r + m_\theta \cos\theta_r + \frac{m_z}{Bo}\frac{\partial \kappa^{(0)}}{\partial z} + \frac{m_\theta}{Bo\, R}\frac{\partial \kappa^{(0)}}{\partial \theta}\Bigg) \\ & + \frac{\kappa^{(1)}}{Bo\left(1 + m_\theta^2 + m_z^2\right)}. \end{aligned} \tag{A.35}$$

At $\mathcal{O}(\epsilon^2)$ for the pressure and $\mathcal{O}(\epsilon)$ for the velocities,

$$\frac{\partial u^{(1)}}{\partial y} = m_\theta \frac{\partial v^{(1)}}{\partial y} + m_z \frac{\partial w^{(1)}}{\partial y} - \frac{\partial w^{(0)}}{\partial z} - \frac{1}{R}\frac{\partial v^{(0)}}{\partial \theta} - \frac{u^{(0)}}{R} - \frac{y\, m_\theta}{R}\frac{\partial v^{(0)}}{\partial \theta}, \tag{A.36}$$

$$\begin{aligned}\frac{\partial p^{(2)}}{\partial y} = &-\frac{1}{R^2}\frac{\partial^2 R}{\partial \theta^2}\frac{\partial u^{(0)}}{\partial \theta} + \frac{1}{R}\frac{\partial u^{(0)}}{\partial y} + \frac{2y}{R}\left(\sin\theta_r - \frac{\partial p^{(1)}}{\partial y} + \left(1+m_z^2\right)\frac{\partial^2 u^{(0)}}{\partial y^2}\right) + 3y\,W^2 \\ &- \frac{\partial^2 R}{\partial z^2}\frac{\partial u^{(0)}}{\partial y} - 2m_z\frac{\partial}{\partial z}\left(\frac{\partial u^{(0)}}{\partial y}\right) + \left(1+m_\theta^2+m_z^2\right)\frac{\partial^2 u^{(1)}}{\partial y^2} + \frac{2m_\theta}{R}\frac{\partial v^{(0)}}{\partial y} - \frac{2m_\theta}{R}\frac{\partial}{\partial \theta}\left(\frac{\partial u^{(0)}}{\partial y}\right),\end{aligned} \tag{A.37}$$

$$\begin{aligned}\left(1+m_\theta^2+m_z^2\right)\frac{\partial^2 v^{(1)}}{\partial y^2} = &-\frac{y}{R}\left(2\left(1+m_z^2\right)\frac{\partial^2 v^{(0)}}{\partial y^2} - 2\cos\theta_r - \frac{1}{R}\frac{\partial p^{(0)}}{\partial \theta} + R\,m_\theta\frac{\partial p^{(1)}}{\partial y}\right) \\ &+ \frac{1}{R}\frac{\partial p^{(1)}}{\partial \theta} - m_\theta\frac{\partial p^{(2)}}{\partial y} + \frac{2m_\theta}{R}\frac{\partial u^{(0)}}{\partial y} - \left(\frac{1}{R} - \frac{\partial^2 R}{\partial z^2} - \frac{1}{R^2}\frac{\partial^2 R}{\partial \theta^2}\right)\frac{\partial v^{(0)}}{\partial y} \\ &+ 2m_z\frac{\partial}{\partial z}\left(\frac{\partial v^{(0)}}{\partial y}\right) + \frac{2\,m_\theta}{R}\frac{\partial}{\partial \theta}\left(\frac{\partial v^{(0)}}{\partial y}\right),\end{aligned} \tag{A.38}$$

$$\begin{aligned}\left(1+m_\theta^2+m_z^2\right)\frac{\partial^2 w^{(1)}}{\partial y^2} = &-\frac{y}{R}\left(2\left(1+m_z^2\right) - 2\frac{\partial p^{(0)}}{\partial z} + 2m_z\frac{\partial p^{(1)}}{\partial y} + \frac{y m_z}{R}\frac{\partial p^{(0)}}{\partial y}\right) \\ &+ \frac{\partial p^{(1)}}{\partial z} - m_z\frac{\partial p^{(2)}}{\partial y} - \left(\frac{1}{R} - \frac{\partial^2 R}{\partial z^2} - \frac{1}{R^2}\frac{\partial^2 R}{\partial \theta^2}\right)\frac{\partial w^{(0)}}{\partial y} + 2m_z\frac{\partial}{\partial z}\left(\frac{\partial w^{(0)}}{\partial y}\right) + \frac{2\,m_\theta}{R}\frac{\partial}{\partial \theta}\left(\frac{\partial w^{(0)}}{\partial y}\right).\end{aligned} \tag{A.39}$$

Integrating yields

$$u^{(1)} = m_\theta v^{(1)} + m_z w^{(1)} - \int\left(\frac{\partial w^{(0)}}{\partial z} + \frac{1}{R}\frac{\partial v^{(0)}}{\partial \theta} + \frac{u^{(0)}}{R} + \frac{y\,m_\theta}{R}\frac{\partial v^{(0)}}{\partial \theta}\right)dy, \tag{A.40}$$

$$\begin{aligned}v^{(1)} = &\, f_{v,1}(y,\theta,z,t)W^2 + f_{v,2}(y,\theta,z,t)\sin\theta_r + f_{v,3}(y,\theta,z,t)\cos\theta_r \\ &+ f_{v,4}(y,\theta,z,t)\frac{\partial \kappa^{(0)}}{\partial \theta} + f_{v,5}(y,\theta,z,t)\frac{\partial \kappa^{(0)}}{\partial z} + f_{v,6}(y,\theta,z,t)\frac{\partial^2 \kappa^{(0)}}{\partial \theta^2} + f_{v,7}(y,\theta,z,t)\frac{\partial^2 \kappa^{(0)}}{\partial z^2} \\ &+ f_{v,8}(y,\theta,z,t)\frac{\partial}{\partial \theta}\left(\frac{\partial \kappa^{(0)}}{\partial z}\right) + f_{v,9}(y,\theta,z,t)\frac{\partial \kappa^{(1)}}{\partial \theta} + f_{v,10}(y,\theta,z,t)\frac{\partial \kappa^{(1)}}{\partial z},\end{aligned} \tag{A.41}$$

$$
\begin{aligned}
w^{(1)} &= f_{w,1}(y,\theta,z,t)W^2 + f_{w,2}(y,\theta,z,t)\sin\theta_r + f_{w,3}(\theta,z,t)\cos\theta_r \\
&+ f_{w,4}(y,\theta,z,t)\frac{\partial\kappa^{(0)}}{\partial\theta} + f_{w,5}(y,\theta,z,t)\frac{\partial\kappa^{(0)}}{\partial z} + f_{w,6}(y,\theta,z,t)\frac{\partial^2\kappa^{(0)}}{\partial\theta^2} + f_{w,7}(y,\theta,z,t)\frac{\partial^2\kappa^{(0)}}{\partial z^2} \\
&+ f_{w,8}(y,\theta,z,t)\frac{\partial}{\partial\theta}\left(\frac{\partial\kappa^{(0)}}{\partial z}\right) + f_{w,9}(y,\theta,z,t)\frac{\partial\kappa^{(1)}}{\partial\theta} + f_{w,10}(y,\theta,z,t)\frac{\partial\kappa^{(1)}}{\partial z}.
\end{aligned} \tag{A.42}
$$

The twenty terms represented by $f_{v,i}$ and $f_{w,i}$ are large, but straightforward to obtain using Mathematica.

A.2 Evolution Equation

To derive the evolution equation, we apply an interfacial mass balance at the liquid-air interface (2.7),

$$
\epsilon\left(R+\epsilon h\right)\frac{\partial h}{\partial t} - \left(R+\epsilon h\right)u + \frac{\partial R+\epsilon h}{\partial\theta}v + \left(R+\epsilon h\right)\frac{\partial R+\epsilon h}{\partial z}w = 0. \tag{A.43}
$$

The continuity equation may be used to express the radial velocity u in terms of the angular velocity v and the axial velocity w,

$$
\begin{aligned}
\left(R+\epsilon h\right)u = \frac{\partial R}{\partial\theta}v(y=h) + \left(R+\epsilon h\right)\frac{\partial R}{\partial z}w(y=h) - \epsilon\frac{\partial R}{\partial z}\int_0^h w\,dy \\
- \epsilon\int_0^h\left(\frac{\partial v}{\partial\theta} + \left(R+\epsilon y\right)\frac{\partial w}{\partial z}\right)dy,
\end{aligned} \tag{A.44}
$$

where integration by parts is used to obtain some expressions related to the axial velocity w. Plugging this into (A.43) yields

$$
\begin{aligned}
\epsilon\left(R+\epsilon h\right)\frac{\partial h}{\partial t} = v\frac{\partial R}{\partial\theta} + w\left(R+\epsilon h\right)\frac{\partial R}{\partial z} - v\frac{\partial R}{\partial\theta} - w\left(R+\epsilon h\right)\frac{\partial R}{\partial z} - \epsilon\frac{\partial h}{\partial\theta}v - \epsilon\left(R+\epsilon h\right)\frac{\partial h}{\partial z}w \\
- \epsilon\frac{\partial R}{\partial z}\int_0^h w\,dy - \epsilon\int_0^h\left(\frac{\partial v}{\partial\theta} + \left(R+\epsilon y\right)\frac{\partial w}{\partial z}\right)dy.
\end{aligned} \tag{A.45}
$$

Combining like terms and dividing by ϵ yields

$$
\left(R+\epsilon h\right)\frac{\partial h}{\partial t} = -\frac{\partial h}{\partial\theta}v - \left(R+\epsilon h\right)\frac{\partial h}{\partial z}w - \frac{\partial R}{\partial z}\int_0^h w\,dy - \int_0^h\left(\frac{\partial v}{\partial\theta} + \left(R+\epsilon y\right)\frac{\partial w}{\partial z}\right)dy. \tag{A.46}
$$

We can apply the Leibniz rule

$$
\begin{aligned}
\int_0^h\frac{\partial}{\partial z}\left(\left(R+\epsilon y\right)w\right)dy &= \frac{\partial R}{\partial z}\int_0^h w\,dy + \int_0^h\left(R+\epsilon y\right)\frac{\partial w}{\partial z}\,dy \\
&= -\left(R+\epsilon h\right)\frac{\partial h}{\partial z}w + \frac{\partial}{\partial z}\left(\int_0^h\left(R+\epsilon y\right)w\,dy\right),
\end{aligned} \tag{A.47}
$$

$$\int_0^h \frac{\partial v}{\partial \theta}\, dy = -v\frac{\partial h}{\partial \theta} + \frac{\partial}{\partial \theta}\left(\int_0^h v\, dy\right), \tag{A.48}$$

which is used to simplify (A.46),

$$(R+\epsilon h)\,\frac{\partial h}{\partial t} = -\frac{\partial}{\partial z}\left(\int_0^h (R+\epsilon y)\, w\, dy\right) - \frac{\partial}{\partial \theta}\left(\int_0^h v\, dy\right). \tag{A.49}$$

Evaluating the integrals in (A.49) yields the evolution equation below, where terms of $\mathcal{O}(\epsilon^2)$ and smaller have been neglected

$$(R+\epsilon h)\,\frac{\partial h}{\partial t} = -\frac{\partial}{\partial z}\left(\int_0^h \left((R+\epsilon y)\, w^{(0)} + \epsilon R w^{(1)}\right) dy\right) - \frac{\partial}{\partial \theta}\left(\int_0^h \left(v^{(0)} + \epsilon v^{(1)}\right) dy\right). \tag{A.50}$$

Evaluating the integrals of $(R+\epsilon y)\, w^{(0)}$ and $v^{(0)}$ yields

$$\begin{aligned}\int_0^h v^{(0)} dy = -\frac{h^3}{3\left(1+m_\theta^2+m_z^2\right)^2}\Bigg(&\frac{1+m_z^2}{Bo\,R}\frac{\partial \kappa^{(0)}}{\partial \theta} + \left(1+m_z^2\right)\cos\theta_r \\ &-W^2 R m_\theta + \sin\theta_r m_\theta - \frac{m_\theta m_z}{Bo}\frac{\partial \kappa^{(0)}}{\partial z}\Bigg)\end{aligned} \tag{A.51}$$

$$\begin{aligned}\int_0^h (R+\epsilon y)\, w^{(0)} dy = -\frac{R\,h^3 + 5h^4/8}{3\left(1+m_\theta^2+m_z^2\right)^2}\Bigg(&m_z \sin\theta_r - m_\theta m_z \cos\theta_r - W^2 R\, m_z \\ &+\frac{1+m_\theta^2}{Bo}\frac{\partial \kappa^{(0)}}{\partial z} - \frac{m_\theta m_z}{Bo}\frac{\partial \kappa^{(0)}}{\partial \theta}\Bigg)\end{aligned} \tag{A.52}$$

Evaluating the integrals of $Rw^{(1)}$ and $v^{(1)}$ is carried out by integrating the constants $f_{w,i}$ and $f_{v,i}$ (Eqns. (A.41) and (A.42)), yielding

$$\begin{aligned}\int_0^h f_{v,1}(y,\theta,z,t)\, dy = &\frac{h^3}{3\left(1+m_\theta^2+m_z^2\right)^4}\left(\left(1+m_\theta^2+m_z^2\right)\left(1+m_z^2\right)\frac{\partial h}{\partial \theta} + \left(1-m_\theta^2+m_z^2\right)\frac{\partial h}{\partial z}\right) \\ &- \frac{h^4}{12\left(1+m_\theta^2+m_z^2\right)^5}\Bigg(m_\theta\left(1+m_z^2\right)\left[\frac{6\left(1+m_z^2\right)}{R}\frac{\partial^2 R}{\partial \theta^2} + m_z m_\theta\left(21\frac{\partial}{\partial \theta}\left(\frac{\partial R}{\partial z}\right) + 5R m_\theta \frac{\partial h}{\partial z}\right)\right] \\ &+ m_z\left(1+m_z^2\right)\left[12R m_\theta m_z \frac{\partial^2 R}{\partial z^2} + \left(1+m_z^2\right)\left(3\frac{\partial}{\partial \theta}\left(\frac{\partial R}{\partial z}\right) + 5R m_\theta \frac{\partial h}{\partial z}\right)\right] \\ &+ 6m_\theta^3\left(m_z m_\theta \frac{\partial}{\partial \theta}\left(\frac{\partial R}{\partial z}\right) + \frac{2}{R}\frac{\partial^2 R}{\partial \theta^2}\left(1+m_z^2\right)\right) - 6m_\theta\left(1+m_z^2\right)^3 - 38m_\theta^5\left(1+m_z^2\right) - 16m_\theta^7 \\ &+ \frac{6m_\theta^5}{R}\frac{\partial^2 R}{\partial \theta^2} - 4m_\theta^3\left(7+17m_z^2+10m_z^4\right)\Bigg) + \frac{4h^5 m_z\left(1+m_z^2\right)}{15R\left(1+m_\theta^2+m_z^2\right)^5}\Bigg(m_\theta m_z\left(1+m_z^2\right) + \\ &-3m_\theta^3 m_z + 3m_\theta^2\frac{\partial}{\partial \theta}\left(\frac{\partial R}{\partial z}\right) + 4R\, m_\theta m_z \frac{\partial^2 R}{\partial z^2} - \left(1+m_z^2\right)\frac{\partial}{\partial \theta}\left(\frac{\partial R}{\partial z}\right)\Bigg)\end{aligned} \tag{A.53}$$

$$\int_0^h f_{w,1}\left(y,\theta,z,t\right)dy = \frac{R\,h^3}{3\left(1+m_\theta^2+m_z^2\right)^4}\left(\left(1+m_z^2+m_\theta^4-m_\theta^2m_z^2+2m_\theta^2\right)\frac{\partial h}{\partial z}\right.$$
$$-\frac{m_\theta^3m_z+m_\theta m_z+m_\theta m_z^3}{R}\frac{\partial h}{\partial\theta}\Bigg)+\frac{h^4}{24\left(1+m_\theta^2+m_z^2\right)^5}\left(11m_z\left(1+m_z^2\right)^3+53m_\theta^2\left(1+m_z^2\right)^2\right.$$
$$-12Rm_z\left(1+m_z^2\right)^2\frac{\partial^2R}{\partial z^2}+m_\theta^4m_z\left(73+49m_z^2\right)+31m_zm_\theta^6-12m_\theta^5\frac{\partial}{\partial\theta}\left(\frac{\partial R}{\partial z}\right)$$
$$-2m_\theta^3\left[6Rm_zm_\theta\frac{\partial^2R}{\partial z^2}+12\frac{\partial}{\partial\theta}\left(\frac{\partial R}{\partial z}\right)+m_z^2\left(3\frac{\partial}{\partial\theta}\left(\frac{\partial R}{\partial z}\right)-5Rm_\theta\frac{\partial h}{\partial z}\right)\right]$$
$$-2m_\theta\left[12Rm_zm_\theta\frac{\partial^2R}{\partial z^2}+6\frac{\partial}{\partial\theta}\left(\frac{\partial R}{\partial z}\right)-5m_z^2\left(Rm_\theta\frac{\partial h}{\partial z}-3\frac{\partial}{\partial\theta}\left(\frac{\partial R}{\partial z}\right)\right)\right.$$
$$\left.\left.-m_z^4\left(5Rm_\theta\frac{\partial h}{\partial z}-9\frac{\partial}{\partial\theta}\left(\frac{\partial R}{\partial z}\right)\right)\right]\right)$$
$$+\frac{4h^5m_z^2m_\theta}{15\left(1+m_\theta^2+m_z^2\right)^5}\left(4m_\theta^3m_z-3m_\theta^2\frac{\partial}{\partial\theta}\left(\frac{\partial R}{\partial z}\right)+\left(1+m_z^2\right)\frac{\partial}{\partial\theta}\left(\frac{\partial R}{\partial z}\right)-4R\,m_zm_\theta\frac{\partial^2R}{\partial z^2}\right) \tag{A.54}$$

$$\int_0^h f_{v,2}\left(y,\theta,z,t\right)dy = \frac{h^3}{3R\left(1+m_\theta^2+m_z^2\right)^4}\left(\left(1+m_z^2\right)\left(1+m_\theta^2+m_z^2\right)\frac{\partial h}{\partial\theta}\right.$$
$$\left.+Rm_\theta m_z\left(1+m_z^2-m_\theta^2\right)\frac{\partial h}{\partial z}\right)$$
$$-\frac{h^4}{12R\left(1+m_\theta^2+m_z^2\right)^5}\left(m_\theta\left(m_z^6-3m_z^2-2\right)-m_\theta^3\left(16+41m_z^2+25m_z^4\right)\right.$$
$$-26m_\theta^5\left(1+m_z^2\right)-12m_\theta^7+\frac{6m_\theta}{R}\frac{\partial^2R}{\partial\theta^2}+6m_\theta^3\left(m_\theta m_z\frac{\partial}{\partial\theta}\left(\frac{\partial R}{\partial z}\right)+\frac{2\left(1+m_z^2\right)}{R}\frac{\partial^2R}{\partial\theta^2}\right)$$
$$m_z\left(1+m_z^2\right)\left(12Rm_\theta m_z\frac{\partial^2R}{\partial z^2}+\left(1+m_z^2\right)\left(3\frac{\partial}{\partial\theta}\left(\frac{\partial R}{\partial z}\right)+5Rm_\theta\frac{\partial h}{\partial z}\right)\right)$$
$$\left.m_\theta\left(1+m_z^2\right)\left(\frac{6\left(1+m_z^2\right)}{R}\frac{\partial^2R}{\partial\theta^2}+m_\theta m_z\left(21\frac{\partial}{\partial\theta}\left(\frac{\partial R}{\partial z}\right)+5Rm_\theta\frac{\partial h}{\partial z}\right)\right)\right)$$
$$\frac{4h^5m_z\left(1+m_z^2\right)}{15\left(1+m_\theta^2+m_z^2\right)^5}\left(m_\theta m_z\left(1+m_z^2\right)-3m_\theta^3m_z+3m_\theta^2\frac{\partial}{\partial\theta}\left(\frac{\partial R}{\partial z}\right)\right.$$
$$\left.\left.+\left(4Rm_\theta m_z\frac{\partial^2R}{\partial z^2}-\left(1+m_z^2\right)\frac{\partial}{\partial\theta}\left(\frac{\partial R}{\partial z}\right)\right)\right)\right) \tag{A.55}$$

$$
\begin{aligned}
\int_0^h f_{w,2}\left(y,\theta,z,t\right)dy = \frac{h^3}{3\left(1+m_\theta^2+m_z^2\right)^4}\Bigg(&\left(1+m_z^2\right)\frac{\partial h}{\partial z}+m_\theta^3\left(m_\theta\frac{\partial h}{\partial z}-\frac{m_z}{R}\frac{\partial h}{\partial \theta}\right)\\
&-m_\theta\left(Rm_\theta\left(m_z^2-2\right)\frac{\partial h}{\partial z}+\frac{m_z\left(1+m_z^2\right)}{R}\frac{\partial h}{\partial \theta}\right)\Bigg)\\
-\frac{h^4}{12R\left(1+m_\theta^2+m_z^2\right)^5}\Bigg(&Rm_z\left(1+m_z^2\right)^2\frac{\partial^2 R}{\partial z^2}-m_\theta^2 m_z\left(10+23m_z^2+13m_z^4\right)\\
&6m_\theta^5\frac{\partial}{\partial\theta}\left(\frac{\partial R}{\partial z}\right)-10m_\theta^6 m_z-m_\theta^4 m_z\left(20+11m_z^2\right)+5m_\theta m_z^2\left(3\frac{\partial}{\partial\theta}\left(\frac{\partial R}{\partial z}\right)-Rm_\theta\frac{\partial h}{\partial z}\right)\\
&+m_\theta^3\left(6Rm_\theta m_z\frac{\partial^2 R}{\partial z^2}+12\frac{\partial}{\partial\theta}\left(\frac{\partial R}{\partial z}\right)+m_z^2\left(3\frac{\partial}{\partial\theta}\left(\frac{\partial R}{\partial z}\right)-5Rm_\theta\frac{\partial h}{\partial z}\right)\right)\\
&+m_\theta\left(12Rm_\theta m_z\frac{\partial^2 R}{\partial z^2}+6\frac{\partial}{\partial\theta}\left(\frac{\partial R}{\partial z}\right)+m_z^4\left(9\frac{\partial}{\partial\theta}\left(\frac{\partial R}{\partial z}\right)-5Rm_\theta\frac{\partial h}{\partial z}\right)\right)\Bigg)\\
+\frac{4h^5 m_\theta m_z^2}{15R\left(1+m_\theta^2+m_z^2\right)^5}\Bigg(&3m_z m_\theta^3-3m_\theta^2\frac{\partial}{\partial\theta}\left(\frac{\partial R}{\partial z}\right)-m_\theta m_z\left(1+m_z^2\right)\\
&-4Rm_\theta m_z\frac{\partial^2 R}{\partial z^2}+\left(1+m_z^2\right)\frac{\partial}{\partial\theta}\left(\frac{\partial R}{\partial z}\right)\Bigg)
\end{aligned}
\tag{A.56}
$$

$$
\begin{aligned}
\int_0^h f_{v,3}\left(y,\theta,z,t\right)dy = \frac{h^3}{6\left(1+m_\theta^2+m_z^2\right)^4}\Bigg(&3m_z\left(1+m_z^2\right)^2\frac{\partial h}{\partial z}-\frac{2m_\theta}{R}\left(1+m_z^2\right)^2\frac{\partial h}{\partial\theta}\\
&+m_\theta^3\left(m_\theta m_z\frac{\partial h}{\partial z}-\frac{2}{R}\frac{\partial h}{\partial\theta}-\frac{2m_z^2}{R}\frac{\partial h}{\partial\theta}\right)\Bigg)\\
-\frac{h^4}{24R\left(1+m_\theta^2+m_z^2\right)^5}\Bigg(&3Rm_\theta^2\left(1+m_z^2\right)\left(3m_\theta^2\frac{\partial^2 R}{\partial z^2}+\frac{8}{R}\left(\frac{1+m_z^2}{R}\frac{\partial^2 R}{\partial\theta^2}-m_\theta m_z\frac{\partial}{\partial\theta}\left(\frac{\partial R}{\partial z}\right)\right)\right)\\
&-12\left(1+m_z^2\right)^3-4m_\theta^2\left(1+m_z^2\right)^2\left(14+11m_z^2\right)-4m_\theta^4\left(19+29m_z^2+10m_z^4\right)-m_\theta^2\left(8+5m_z^2\right)\\
&+3R\left(m_\theta^6\frac{\partial^2 R}{\partial z^2}+\frac{4m_\theta^4}{R}\left(\frac{1+m_z^2}{R}\frac{\partial^2 R}{\partial\theta^2}-m_\theta m_z\frac{\partial}{\partial\theta}\left(\frac{\partial R}{\partial z}\right)\right)\right)\\
&+\left(1+m_z^2\right)^2\left(10m_z\left(1+m_z^2\right)\frac{\partial h}{\partial z}+3\left(1+5m_z^2\right)\frac{\partial^2 R}{\partial z^2}\right)-3m_\theta^2\left(1+m_z^2\right)\left(m_z^2-3\right)\frac{\partial^2 R}{\partial z^2}\\
&+2\left(1+m_z^2\right)^2\left(\frac{6\left(1+m_z^2\right)}{R^2}\frac{\partial^2 R}{\partial\theta^2}+m_\theta m_z\left(\frac{6}{R}\frac{\partial}{\partial\theta}\left(\frac{\partial R}{\partial z}\right)+5m_\theta\frac{\partial h}{\partial z}\right)\right)\Bigg)\\
+\frac{8h^5 m_z\left(1+m_z^2\right)}{15R\left(1+m_\theta^2+m_z^2\right)^5}\Bigg(&\left(Rm_z\frac{\partial^2 R}{\partial z^2}-2m_\theta^2 m_z\right)\left(1+m_z^2\right)\\
&+m_\theta\left(2\left(1+m_z^2\right)\frac{\partial}{\partial\theta}\left(\frac{\partial R}{\partial z}\right)-Rm_\theta m_z\frac{\partial^2 R}{\partial z^2}\right)\Bigg)
\end{aligned}
\tag{A.57}
$$

$$\int_0^h f_{w,3}\left(y,\theta,z,t\right)dy = \frac{h^3}{6R^8\left(1+m_\theta^2+m_z^2\right)^4}\left(m_\theta^4\left(\frac{3m_z}{R}\frac{\partial h}{\partial\theta}-2m_\theta\frac{\partial h}{\partial z}\right)\right.$$
$$-2m_\theta^2\left(m_\theta\left(2+m_z^2\right)\frac{\partial h}{\partial z}-\frac{2m_z\left(1+m_z^2\right)}{R}\frac{\partial h}{\partial\theta}\right)$$
$$\left.\left(1+m_z^2\right)\left(\frac{m_z\left(1+m_z^2\right)}{R}\frac{\partial h}{\partial\theta}-2m_\theta\left(1+2m_z^2\right)\frac{\partial h}{\partial z}\right)\right)$$
$$+\frac{h^4}{24R\left(1+m_\theta^2+m_z^2\right)^5}\left(5m_\theta m_z\left(1+m_z^2\right)^3-m_\theta^3m_z\left(5+34m_z^2+29m_z^4\right)\right.$$
$$-25m_\theta^5m_z\left(1+m_z^2\right)-15m_\theta^7m_z+3m_\theta^6\frac{\partial}{\partial\theta}\left(\frac{\partial R}{\partial z}\right)-3m_\theta\left(\left(1+m_z^2\right)\frac{\partial}{\partial\theta}\left(\frac{\partial R}{\partial z}\right)-4Rm_\theta m_z\frac{\partial^2R}{\partial z^2}\right)$$
$$\left(1+m_z^2\right)\left(Rm_\theta m_z\left(12+24m_z^2\right)\frac{\partial^2R}{\partial z^2}-9\frac{\partial}{\partial\theta}\left(\frac{\partial R}{\partial z}\right)-m_z^2\left(18+9m_z^2\right)\frac{\partial}{\partial\theta}\left(\frac{\partial R}{\partial z}\right)\right.$$
$$+10Rm_\theta m_z^2\left(1+m_z^2\right)\frac{\partial h}{\partial z}\Big)+m_\theta^2\left(12Rm_\theta m_z\left(2+m_z^2\right)\frac{\partial^2R}{\partial z^2}-15\frac{\partial}{\partial\theta}\left(\frac{\partial R}{\partial z}\right)\right.$$
$$\left.\left.+10Rm_\theta m_z^2\left(1+m_z^2\right)\frac{\partial h}{\partial z}+m_z^2\left(9m_z^2-6\right)\frac{\partial}{\partial\theta}\left(\frac{\partial R}{\partial z}\right)\right)\right)$$
$$-\frac{8m_z^2m_\theta h^5}{15\left(1+m_\theta^2+m_z^2\right)^5}\left(m_z\left(1+m_z^2\right)\frac{\partial^2R}{\partial z^2}-2m_\theta^2m_z\left(1+m_z^2\right)\right.$$
$$\left.+m_\theta\left(\frac{2\left(1+m_z^2\right)}{R}\frac{\partial}{\partial\theta}\left(\frac{\partial R}{\partial z}\right)-m_\theta m_z\frac{\partial^2R}{\partial z^2}\right)\right) \tag{A.58}$$

$$\int_0^h f_{v,4}\left(y,\theta,z,t\right)dy = \frac{h^3\left(\left(1+m_z^2\right)^2\left(2m_\theta\frac{\partial h}{\partial\theta}-3Rm_z\frac{\partial h}{\partial z}\right)+m_z^3\left(2\left(1+m_z^2\right)\frac{\partial h}{\partial\theta}-Rm_\theta m_z\frac{\partial h}{\partial z}\right)\right)}{6BoR^2\left(1+m_\theta^2+m_z^2\right)^4}$$
$$+\frac{h^4}{24BoR^2\left(1+m_\theta^2+m_z^2\right)^5}\left(\left(1+m_z^2\right)^3\left(11m_z^2-4\right)-m_\theta^2\left(1+m_z^2\right)^2\left(32+23m_z^2\right)\right.$$
$$-m_\theta^4\left(52+77m_z^2+25m_\theta^4\right)-3m_\theta^6\left(8+5m_z^2\right)+3\left(Rm_\theta^6\frac{\partial^2R}{\partial z^2}+4m_\theta^4\left(\frac{1+m_z^2}{R}\frac{\partial^2R}{\partial\theta^2}-m_\theta m_z\frac{\partial}{\partial\theta}\left(\frac{\partial R}{\partial z}\right)\right)\right)$$
$$+3m_\theta^2\left(1+m_z^2\right)\left(3Rm_\theta^2\frac{\partial^2R}{\partial z^2}+8\left(\frac{1+m_z^2}{R}\frac{\partial^2R}{\partial\theta^2}-m_\theta m_z\frac{\partial}{\partial\theta}\left(\frac{\partial R}{\partial z}\right)\right)\right)$$
$$+R\left(1+m_z^2\right)^2\left(3\left(1+5m_z^2\right)\frac{\partial^2R}{\partial z^2}+10m_z\left(1+m_z^2\right)\frac{\partial h}{\partial z}\right)$$
$$\left.-\left(1+m_z^2\right)\left(3Rm_\theta^2\left(m_z^2-3\right)\frac{\partial^2R}{\partial z^2}-2\left(1+m_z^2\right)\left(\frac{6\left(1+m_z^2\right)}{R}\frac{\partial^2R}{\partial\theta^2}+m_\theta m_z\left(6\frac{\partial}{\partial\theta}\left(\frac{\partial R}{\partial z}\right)+5Rm_\theta\frac{\partial h}{\partial z}\right)\right)\right)\right)$$
$$-\frac{4h^5m_z\left(1+m_z^2\right)}{15BoR^2\left(1+m_\theta^2+m_z^2\right)^5}\left(m_z\left(1+m_z^2\right)^2+2Rm_z\left(1+m_z^2\right)\frac{\partial^2R}{\partial z^2}-3m_\theta^2m_z\left(1+m_z^2\right)\right.$$
$$\left.+2m_\theta\left(\frac{2}{R}\left(1+m_z^2\right)\frac{\partial}{\partial\theta}\left(\frac{\partial R}{\partial z}\right)-Rm_\theta m_z\frac{\partial^2R}{\partial z^2}\right)\right) \tag{A.59}$$

$$\begin{aligned}\int_0^h f_{w,4}\left(y,\theta,z,t\right)dy = \frac{h^3}{6BoR^2\left(1+m_\theta^2+m_z^2\right)^4}\Bigg(m_\theta^4\left(2Rm_\theta\frac{\partial h}{\partial z}-3m_z\frac{\partial h}{\partial\theta}\right)\\ +2m_\theta^2\left(Rm_\theta\left(2+m_z^2\right)\frac{\partial h}{\partial z}-2m_z\left(1+m_z^2\right)\frac{\partial h}{\partial\theta}\right)\\ -\left(1+m_z^2\right)\left(m_z\left(1+m_z^2\right)\frac{\partial h}{\partial\theta}-2Rm_\theta\left(1+2m_z^2\right)\frac{\partial h}{\partial z}\right)\Bigg)\\ -\frac{h^4}{24BoR^2\left(1+m_\theta^2+m_z^2\right)^5}\Big(2m_\theta m_z\left(1+m_z^2\right)^2\left(5+8m_z^2\right)+2m_\theta^3m_z\left(5+m_z^2-4m_z^4\right)\\ -10m_\theta^5m_z\left(1+m_z^2\right)-10m_\theta^7m_z+3m_\theta^6\frac{\partial}{\partial\theta}\left(\frac{\partial R}{\partial z}\right)\\ -3m_\theta^4\left(\left(1+m_z^2\right)\frac{\partial}{\partial\theta}\left(\frac{\partial R}{\partial z}\right)-4Rm_\theta m_z\frac{\partial^2R}{\partial z^2}\right)\\ +\left(1+m_z^2\right)\left(12Rm_\theta m_z\frac{\partial^2R}{\partial z^2}\left(1+2m_z^2\right)-9\frac{\partial}{\partial\theta}\left(\frac{\partial R}{\partial z}\right)\left(1+m_z^2\right)^2+10m_z^2Rm_\theta\left(1+m_z^2\right)\frac{\partial h}{\partial z}\right)\\ +m_\theta^2\left(12Rm_\theta m_z\left(2+m_z^2\right)\frac{\partial^2R}{\partial z^2}-\frac{\partial}{\partial\theta}\left(\frac{\partial R}{\partial z}\right)\left(15+6m_z^2-9m_z^4\right)+10Rm_\theta m_z^2\left(1+m_z^2\right)\frac{\partial h}{\partial z}\right)\Big)\\ +\frac{4h^5m_\theta m_z^2}{15BoR^2\left(1+m_\theta^2+m_z^2\right)^5}\Bigg(m_z\left(1+m_z^2\right)^2+2Rm_z\left(1+m_z^2\right)\frac{\partial^2R}{\partial z^2}-3m_\theta^2m_z\left(1+m_z^2\right)\\ +2m_\theta\left(\frac{2}{R}\left(1+m_z^2\right)\frac{\partial}{\partial\theta}\left(\frac{\partial R}{\partial z}\right)-Rm_\theta m_z\frac{\partial^2R}{\partial z^2}\right)\Bigg)\end{aligned} \tag{A.60}$$

$$\int_0^h f_{v,5}\left(y,\theta,z,t\right)dy = \frac{h^3}{6BoR\left(1+m_\theta^2+m_z^2\right)^4}\left(2m_\theta^2\left(m_z\left(1+m_z^2\right)\frac{\partial h}{\partial\theta} - Rm_\theta\left(1+2m_z^2\right)\frac{\partial h}{\partial z}\right)\right.$$
$$\left. -Rm_\theta^5\frac{\partial h}{\partial z} + \left(1+m_z^2\right)\left(2m_z\left(1+m_z^2\right)\frac{\partial h}{\partial\theta} + Rm_\theta\left(m_z^2-1\right)\frac{\partial h}{\partial z}\right)\right)$$
$$- \frac{h^4}{24Bo\left(1+m_\theta^2+m_z^2\right)^5}\left(m_\theta m_z\left(1+m_z^2\right)^2\left(5+11m_z^2\right) - 5m_\theta^3 m_z\left(5+28m_z^2+23m_z^4\right)\right.$$
$$- 25m_\theta^5 m_z\left(1+m_z^2\right) - 15m_\theta^7 m_z + 3m_\theta^5\left(\frac{4m_z}{R}\frac{\partial^2 R}{\partial\theta^2} - 3m_\theta\frac{\partial}{\partial\theta}\left(\frac{\partial R}{\partial z}\right)\right)$$
$$- 3m_\theta^3\left(m_\theta\left(9+5m_z^2\right)\frac{\partial}{\partial\theta}\left(\frac{\partial R}{\partial z}\right)\frac{8m_z\left(1+m_z^2\right)}{R}\frac{\partial^2 R}{\partial\theta^2}\right)$$
$$+ m_\theta\left(1+m_z^2\right)\left(5m_\theta m_z^2\left(3\frac{\partial}{\partial\theta}\left(\frac{\partial R}{\partial z}\right) + 2Rm_\theta\frac{\partial h}{\partial z}\right) + \frac{12m_z^3}{R}\frac{\partial^2 R}{\partial\theta^2} - 27m_\theta\frac{\partial}{\partial\theta}\left(\frac{\partial R}{\partial z}\right)\right.$$
$$-6m_z\left(Rm_\theta^2\frac{\partial^2 R}{\partial z^2} - \frac{2}{R}\frac{\partial^2 R}{\partial\theta^2}\right)\Big) + \left(1+m_z^2\right)\left(6Rm_\theta m_z\left(3m_z^2-1\right)\frac{\partial^2 R}{\partial z^2}\right.$$
$$\left. -3\frac{\partial}{\partial\theta}\left(\frac{\partial R}{\partial z}\right)\left(3+4m_z^2+m_z^4\right) + 10Rm_\theta m_z^2\left(1+m_z^2\right)\frac{\partial h}{\partial z}\right)\Big)$$
$$- \frac{4h^5 m_z\left(1+m_z^2\right)}{15BoR\left(1+m_\theta^2+m_z^2\right)^5}\left(3m_\theta^3 m_z^2 - m_\theta m_z^2\left(1+m_z^2\right)\right.$$
$$\left. +Rm_\theta\left(1-3m_z^2\right)\frac{\partial^2 R}{\partial z^2} + m_z\left(1+m_z^2\right)\frac{\partial}{\partial\theta}\left(\frac{\partial R}{\partial z}\right) + m_\theta^2\left(Rm_\theta\frac{\partial^2 R}{\partial z^2} - 3m_z\frac{\partial}{\partial\theta}\left(\frac{\partial R}{\partial z}\right)\right)\right)$$
(A.61)

$$\int_0^h f_{w,5}\left(y,\theta,z,t\right)dy = \frac{h^3}{6BoR\left(1+m_\theta^2+m_z^2\right)^4}\left(2Rm_z\left(1+m_z^2\right)\frac{\partial h}{\partial z}+m_\theta^5\frac{\partial h}{\partial \theta}\right.$$
$$+2m_\theta^3\left(Rm_\theta m_z\frac{\partial h}{\partial z}+\frac{\partial h}{\partial \theta}\right)+m_\theta\left(2Rm_\theta\left(1-2m_z^2\right)\frac{\partial h}{\partial z}+\left(1-m_z^4\right)\frac{\partial h}{\partial \theta}\right)\Big)$$
$$+\frac{h^4}{24BoR\left(1+m_\theta^2+m_z^2\right)^5}\left(12R\left(1+m_z^2\right)\frac{\partial^2 R}{\partial z^2}-3\left(1+m_z^2\right)^3\right.$$
$$+m_\theta^2\left(16m_z^6+7m_z^4-28m_z^2-19\right)-m_\theta^4\left(39+29m_z^2+8m_z^4\right)$$
$$-m_z^6\left(33+10m_z^2\right)-10m_\theta^8+\frac{3m_z^6}{R}\frac{\partial^2 R}{\partial\theta^2}+3m_\theta^4\left(4Rm_\theta^2\frac{\partial^2 R}{\partial z^2}-4m_\theta m_z\frac{\partial}{\partial\theta}\left(\frac{\partial R}{\partial z}\right)+\frac{3\left(1+m_z^2\right)}{R}\frac{\partial^2 R}{\partial\theta^2}\right)$$
$$+m_\theta^2\left(18Rm_\theta^2\left(2+m_z^2\right)\frac{\partial^2 R}{\partial z^2}-24m_\theta m_z\frac{\partial}{\partial\theta}\left(\frac{\partial R}{\partial z}\right)+\frac{9}{R}\left(1+m_z^2\right)^2\frac{\partial^2 R}{\partial z^2}\right.$$
$$\left.+2m_z^3m_\theta\left(5Rm_\theta\frac{\partial h}{\partial z}-3\frac{\partial}{\partial\theta}\left(\frac{\partial R}{\partial z}\right)\right)\right)+6Rm_\theta^2\left(6+7m_z^2+5m_z^4\right)$$
$$\left(1+m_z^2\right)\left(\frac{3\left(1+m_z^2\right)^2}{R}\frac{\partial^2 R}{\partial\theta^2}+2m_\theta m_z^3\left(5Rm_\theta\frac{\partial h}{\partial z}-9\frac{\partial}{\partial\theta}\left(\frac{\partial R}{\partial z}\right)\right)-12m_\theta m_z\frac{\partial}{\partial\theta}\left(\frac{\partial R}{\partial z}\right)\right)\Big)$$
$$-\frac{4h^5m_z^2m_\theta}{15BoR\left(1+m_\theta^2+m_z^2\right)^5}\left(3m_\theta^3m_z^2-m_\theta m_z^2\left(1+m_z^2\right)+m_\theta^2\left(Rm_\theta\frac{\partial^2 R}{\partial z^2}-3m_z\frac{\partial}{\partial\theta}\left(\frac{\partial R}{\partial z}\right)\right)\right.$$
$$\left.+Rm_\theta\left(1-3m_z^2\right)\frac{\partial^2 R}{\partial z^2}+m_z\left(1+m_z^2\right)\frac{\partial}{\partial\theta}\left(\frac{\partial R}{\partial z}\right)\right) \tag{A.62}$$

$$\int_0^h f_{v,6}\left(y,\theta,z,t\right)dy = 0 \tag{A.63}$$

$$\int_0^h f_{w,6}\left(y,\theta,z,t\right)dy = -\frac{h^4m_z}{8BoR^2\left(1+m_\theta^2+m_z^2\right)} \tag{A.64}$$

$$\int_0^h f_{v,7}\left(y,\theta,z,t\right)dy = \frac{h^4\left(m_z\left(m_z^4-1\right)-2m_\theta^3\left(1+m_z^2\right)-m_\theta^5\right)}{8Bo\left(1+m_\theta^2+m_z^2\right)^4}-\frac{4h^5m_\theta m_z^2\left(1+m_z^2\right)}{15Bo\left(1+m_\theta^2+m_z^2\right)^4} \tag{A.65}$$

$$\int_0^h f_{w,7}\left(y,\theta,z,t\right)dy = -\frac{h^4m_z^3m_\theta^2}{4Bo\left(1+m_\theta^2+m_z^2\right)^4}+\frac{4h^5m_z^3m_\theta^2}{15Bo\left(1+m_\theta^2+m_z^2\right)^4} \tag{A.66}$$

$$\int_0^h f_{v,8}\left(y,\theta,z,t\right)dy = -\frac{h^4m_z\left(\left(1+m_z^2\right)^2-2m_\theta^2\left(1+m_z^2\right)-m_\theta^4\right)}{8RBo\left(1+m_\theta^2+m_z^2\right)^4}+\frac{4h^5m_z\left(1+m_z^2\right)^2}{15RBo\left(1+m_\theta^2+m_z^2\right)^4} \tag{A.67}$$

$$\int_0^h f_{w,8}\left(y,\theta,z,t\right)dy = \frac{h^4 m_\theta \left(\left(1+4m_z^2+3m_z^4\right)^2+2m_\theta^2\left(1+m_z^2\right)+m_\theta^4\right)}{8RBo\left(1+m_\theta^2+m_z^2\right)^4} - \frac{4h^5 m_\theta m_z^2\left(1+m_z^2\right)}{15RBo\left(1+m_\theta^2+m_z^2\right)^4} \tag{A.68}$$

$$\int_0^h f_{v,9}\left(y,\theta,z,t\right)dy = \frac{h^3 m_\theta m_z}{3Bo\left(1+m_\theta^2+m_z^2\right)^2} \tag{A.69}$$

$$\int_0^h f_{w,9}\left(y,\theta,z,t\right)dy = -\frac{h^3\left(1+m_\theta^2\right)}{3Bo\left(1+m_\theta^2+m_z^2\right)^2} \tag{A.70}$$

$$\int_0^h f_{v,10}\left(y,\theta,z,t\right)dy = -\frac{h^3}{3BoR\left(1+m_\theta^2+m_z^2\right)^2} \tag{A.71}$$

$$\int_0^h f_{w,10}\left(y,\theta,z,t\right)dy = \frac{h^3 m_\theta m_z}{3BoR\left(1+m_\theta^2+m_z^2\right)^2} \tag{A.72}$$

Appendix B 2D Finite-Element Method

The governing equations (Eqns. (2.20) and (2.21)), along with the boundary conditions (Eqns. (2.5)–(2.9)) are solved using the Galerkin finite-element method and a second-order adaptive time-stepping algorithm [16, 24, 31]. The velocity and pressure are approximated using bi-quadratic and linear discontinuous basis functions, respectively. The flow domain (x, y) is mapped to a reference computational domain (ξ, η), and the unknown position of the elements in the flow domain is solved at each time step using elliptic mesh generation,

$$\nabla\cdot\left(D_\xi\nabla\xi\right)=0, \quad \nabla\cdot\left(D_\eta\nabla\eta\right)=0, \tag{B.1}$$

where D_ξ and D_η are mesh diffusion coefficients. The position of the liquid-air interface is obtained at each timestep using the kinematic condition (Eqn. (2.7)) and the position of the remaining elements is obtained by solving Eqn. (B.1). In the computational domain, orthogonality of the mesh is enforced as an additional boundary condition at the free surface [32].

For each GFEM simulation, the domain is discretized with roughly 4000 elements, with 400 around the cylinder circumference and 10 through the depth of the coating. Given the spatial

and temporal discretization of the governing equations and boundary conditions, the resulting set of nonlinear algebraic equations is solved using the Newton-Rhapson method. The solution for a given timestep is accepted when the norm of the difference between residuals is less than 10^{-8}. Mass conservation is monitored by calculating the variation in the mass of liquid on the cylinder per unit length $\Delta A = 100\left(A_{max} - A_{min}\right)/A_0$, where A_{max} is maximum load of liquid on the cylinder, A_{min} is the minimum load, A_0 is the initial load of liquid, and the load is given by Eqn. (2.19). Results of the GFEM simulations are considered accurate if $\Delta A < 0.1$. Lastly, the film thickness obtained from the GFEM simulations is calculated as a function of the angular coordinate θ as the distance between the free-surface and the cylinder surface along a line of fixed θ. This thickness may then be compared to that calculated using the lubrication-theory-based model presented in §2.2.

References

[1] S.M. Benjamin, S.M. Bennett, J.C. Bew, and J.L. Swank. Process for preparing a sugar coating on an irregular shaped confection, U.S. patent application 20080026131 (31 January 2008).

[2] D.N. Cade and D.H. Xinwe. Hydroxypropyl methyl cellulose hard capsules and process of manufacture, U.S. patent 9,655,860 (23 May 2017).

[3] D. Castro, S. Wu, K.L. Woolbright, K.W. Scheinpflug, S.F. A. Hossainy, and L. Chen. Apparatus and method for depositing a coating onto a surface of a prosthesis, U.S. patent 6,395,326 (28 May 2002).

[4] R.A. Chappa, A.G. Bach, and M. Macgregor. Apparatus and methods for coating medical devices, U.S. patent 9,623,215 (18 April 2017).

[5] Y. Chen and H. Ho. System and method for coating an implantable medical device, U.S. patent 7,563,324 (21 July 2009).

[6] P. Heller, A. Heldman, J. Foehlich, and D. Kim. Method and apparatus for coating an endoprosthesis, U.S. patent application 20030215564 (20 November 2003).

[7] A. Lee, P.T. Brun, J. Marthelot, G. Balestra, F. Gallaire, and P.M. Reis. Fabrication of slender elastic shells by the coating of curved surfaces. *Nature Communications*, 7:11155, 2016.

[8] N. Keefer and B. Bosch. Molded fuel tank and method of manufacturing the same, U.S. patent 10,023,322 (17 July 2018).

[9] N. Fujitaka and A. Kobayashi Rotational-molded resin fuel tank, U.S. patent application 20060068139 (30 March 2006).

[10] P. L. Evans, L. W. Schwartz, and R. V. Roy. Three-dimensional solutions for coating flow on a rotating horizontal cylinder: Theory and experiment. *Physics of Fluids*, 17:072102, 2005.

[11] W. Li and S. Kumar. Three-dimensional surfactant-covered flows of thin liquid films on rotating cylinders. *Journal of Fluid Mechanics*, 844:61–91, 2018.

[12] H.K. Moffatt. Behaviour of a viscous film on the outer surface of a rotating cylinder. *Journal de Mécanique*, 16:651–673, 1977.

[13] V.V. Pukhnachev. Motion of a liquid film on the surface of a rotating cylinder in a gravitational field. *Journal of Applied Mechanics and Technical Physics*, 18:344–351, 1977.

[14] M.A. Kelmanson. Theoretical and experimental analyses of the maximum-supportable fluid load on a rotating cylinder. *Journal of Engineering Mathematics*, 24:1094–1114, 2008.

[15] R. Hunt. Numerical solution of the free-surface viscous flow on a horizontal rotating elliptical cylinder. *Numerical Methods for Partial Differential Equations*, 24:1094–1114, 2008.

[16] W. Li, M. S. Carvalho, and S. Kumar. Viscous free-surafce flows on rotating elliptical cylinders. *Physical Review Fluids*, 2:094005, 2017.

[17] R.V. Roy, A.J. Roberts, and M.E. Simpson. A lubrication model of coating flows over a curved substrate in space. *Journal of Fluid Mechanics*, 24:1094–1114, 2008.

[18] A.J. Roberts and Z. Li. An accurate and comprehensive model of thin fluid flows with inertia on curved substrates. *Journal of Fluid Mechanics*, 553:33–73, 2006.

[19] P.D. Howell. Surface-tension-driven flow on a moving curved surface. *Journal of Engineering Mathematics*, 45:283–308, 2003.

[20] A.W. Wray, D.T. Papageorgiou, and O.K. Matar. Reduced models for thick liquid layers with inertia on highly curved substrates. *SIAM Journal on Applied Mathematics*, 77:881–904, 2017.

[21] A.W. Wray and R. Cimpeanu. Reduced-order modeling of thick inertial flows around rotating cylinders. *Journal of Fluid Mechanics*, 898:A1, 2020.

[22] R. Stocker and A.E. Hosoi. Corner flow in free liquid films. *Journal of Engineering Mathematics*, 50:267–288, 2004.

[23] R. Stocker and A.E. Hosoi. Lubrication in a corner. *Journal of Fluid Mechanics*, 544:353–377, 2005.

[24] W. Li, M.S. Carvalho, and S. Kumar. Liquid-film coating on topographically patterned rotating cylinders. *Physical Review Fluids*, 2:024001, 2017.

[25] C. Parrish, L. Pham, and S. Kumar. Thin-liquid-film flow on three-dimensional topographically patterned rotating cylinders. *Journal of Fluid Mechanics*, 918:A12, 2021.

[26] J.M. Delhaye. Jump conditions and entropy sources in two-phase systems. Local instant formulation. *International Journal of Multiphase Flow*, 1:395–409, 1974.

[27] J.P. Burelbach, S.G. Bankoff, and S.H. Davis. Nonlinear stability of evaporating/condensing liquid films. *Journal of Fluid Mechanics*, 195:463–494, 1988.

[28] J.C. Slattery. *Interfacial transport phenomena*. New York : Springer, New York, 2nd ed., 2007.

[29] P. L. Evans, L. W. Schwartz, and R. V. Roy. Steady and unsteady solutions for coating flow on a rotating horizontal cylinder: Two-dimensional theoretical and numerical modeling. *Physics of Fluids*, 16:2742–2756, 2004.

[30] W. Li and S. Kumar. Thin-film coating of surfactant-laden liquids on rotating cylinders. *Physics of Fluids*, 27:072106, 2015.

[31] S. Dodds, M.S. Carvalho, and S. Kumar. Stretching and slipping of liquid bridges near plates and cavities. *Physics of Fluids*, 21:092103, 2009.

[32] K.N. Christodoulou, S.F. Kistler, and P.R. Schunk. Advances in computational methods for free-surface flows, in Liquid Film Coating, edited by S. F. Kistler and P. M. Schweizer (Springer, Amsterdam, 1997), pp. 297–366.